FAKULTÄT FÜR PHYSIK
Institut für Experimentelle Kernphysik (IEKP)

Simulations of tritium induced background in the KATRIN pre-spectrometer

Masterarbeit
von

Momin Ahmad

Fakultät für Physik
Institut für Experimentelle Kernphysik (IEKP)

Referent:	Prof. Dr. G. Drexlin
Korreferent:	Prof. Dr. W. de Boer
Betreuender Mitarbeiter:	Dr. Fabian Harms

Bearbeitungszeit: 02. November 2015 – 02. November 2016

Erklärung zur Selbstständigkeit

Ich versichere, dass ich diese Arbeit selbstständig verfasst habe und keine anderen als die angegebenen Quellen und Hilfsmittel benutzt habe, die wörtlich oder inhaltlich übernommenen Stellen als solche kenntlich gemacht und die Satzung des KIT zur Sicherung guter wissenschaftlicher Praxis in der gültigen Fassung vom 17.05.2010 beachtet habe.

Karlsruhe, den 02.11.2016, _____

Momin Ahmad

Als Ansichtsexemplar genehmigt von

Karlsruhe, den 02.11.2016, _____

Prof. Dr. G. Drexlin

Simulationen von Tritium-induzierten Untergrund im KATRIN Vorspektrometer

Das **Ka**rlsruher **Tri**tium **N**eutrino Experiment (KATRIN) plant die modellunabhängige Messung der Masse des Elektron-Antineutrinos mit einer Sensitivität von $m_\nu = 200\,\mathrm{meV/c^2}$ (bei 90% C.L.). Für dieses Ziel wird das Energiespektrum vom Tritium-β^--Zerfall Nahe der Endpunktenergie von 18.6 keV untersucht.

In der Quelle entstehen die zu analysierenden Elektronen aus dem β-Zerfall von Tritium. Diese werden anschließend vom anliegenden Magnetfeld zu den Spektrometern geführt und analysiert, bis sie den Detektor erreichen und ein Signal auslösen. Neben den Signal-Elektronen können auch Moleküle (teilweise) aus Tritium in neutraler und ionisierter Form die Quelle verlassen. Neutrales Tritium kann durch Diffusionsprozesse in die Spektrometer gelangen, ionisiertes Tritium wird vom umgebenen Magnetfeld dorthin geführt. Im Spektrometer angekommen kann eine größere Menge von Tritium die Spektrometer kontaminieren und zu einem erheblichen Untergrund beitragen. Um das zu verhindern, sind auf der Strecke zwischen Quelle und Spektrometer Vakuumpumpen angebracht, die den Tritiumfluss reduzieren.
Diese Arbeit überprüft die Möglichkeit, die Funktionsfähigkeit der Vakuumpumpen (z.B. Kryopumpen) zu testen, indem Tritium-β-Zerfälle im Vorspektrometer des KATRIN Experiments gezählt werden. Die daraus resultierende Zerfallsrate gibt Aufschluss über den Zustand der Vakuumpumpen. Eine gestiegene Zerfallsrate wäre zum Beispiel auf eine Verschlechterung der Pumpleistung zurückzuführen. Da ionisierte Moleküle durch das Magnetfeld geführt werden und nicht effizient genug von den Vakuumpumpen entfernt werden können, wird abschließend eine Methode diskutiert, die den Untergrund dieser Ionen minimiert.

Contents

1 Introduction **11**

2 Neutrinos **13**
2.1 Historic Background 13
2.2 Neutrino mass 15
2.2.1 Solar neutrino problem 15
2.2.2 Neutrino oscillation 16
2.2.3 Neutrino oscillation experiments 18
2.3 Measuring the neutrino mass 18
2.3.1 Neutrinos in cosmology 19
2.3.2 Neutrinos from supernovae 20
2.3.3 Neutrinoless double β-decay 20
2.3.4 Neutrino mass from single β-decay 21

3 KATRIN **23**
3.1 Measurement Principle 23
3.2 The MAC-E filter 23
3.2.1 Trapped particles 24
3.2.2 Energy resolution and conservation of the magnetic flux 25
3.3 KATRIN beamline 26
3.3.1 The rear section 26
3.3.2 The WGTS 26
3.3.3 The transport section with DPS and CPS 27
3.3.4 Spectrometer and detector section 27

4 Simulations with KASSIOPEIA **31**
4.1 Starting a simulation 31
4.1.1 Structure of a simulation process 32
4.1.2 Particle generation 32
4.1.3 Propagation of particles 33
4.1.4 Calculating electric and magnetic fields 33
4.1.4.1 Magnetic field calculation 33
4.1.4.2 Electric field calculation 35
4.2 Extending the source code 36
4.2.1 Homogeneous flux tube generator 37
4.2.2 Multiplicity generator 37

5 Stored-particle induced background **41**
5.1 Tritium migration into the CPS 41
5.2 Background characteristics 42
5.3 Detecting β-decays in the PS 44
5.4 Checking the functionality of the CPS 44

5.5 Preparatory simulations . . . 45
5.5.1 Simulation parameters . . . 45
5.5.2 Arrival probability of secondary electron clusters . . . 49
5.6 Outlook for storage simulation . . . 51

6 Storage simulation **53**
6.1 Simulation configuration . . . 53
6.1.1 Generator and terminators . . . 53
6.1.2 Dynamic enhancement . . . 54
6.2 Analysis of simulation data . . . 54
6.2.1 Imitating experimental data . . . 54
6.2.2 Analysis code . . . 55
6.2.2.1 Cluster detection . . . 55
6.2.2.2 Accidental detection . . . 55
6.2.3 Analysis results . . . 57
6.2.3.1 Number of secondary electrons and detection ratio . . . 62
6.3 Discussion of results . . . 62

7 Ion simulation **65**
7.1 Ion generation . . . 65
7.1.1 Molecular ions . . . 66
7.1.2 Recombination of ions . . . 66
7.1.3 Ion currents . . . 67
7.2 Impact of ions . . . 67
7.3 Ion blocking . . . 67
7.4 Summary . . . 70

8 Conclusion **71**

Bibliography **73**

List of Figures

2.1 Solar neutrino flux generated by different nuclear reactions 16
2.2 Normal and inverted neutrino mass hierarchy 19
2.3 Feyman diagram of the neutrinoless double beta decay with energy spectrum. 20
2.4 Feyman diagram of the single $beta^-$-decay with energy spectrum. 22

3.1 MAC-E filter principle. 24
3.2 Penning trap and magnetic-bottle trap. 25
3.3 The experimental setup of KATRIN. 26
3.4 Position and geometry of electrodes in the PS 28
3.5 Schematic overview of the layout of the KATRIN detector wafer 29

4.1 The logo of the KASSIOPEIA program. 31
4.2 KASSIOPEIA simulation structure. 32
4.3 Display of homogeinity in the flux tube 38
4.4 Particles generated with equal magnetic flux values. 39

5.1 Stored β-electron in the PS 43
5.2 Storage time of electrons in the MS at different pressures 43
5.3 Detector hit rate at normal pressure and at elevated pressure. 44
5.4 Theoretical energy spectrum of secondary electrons from tritium decays in the PS 46
5.5 Termination of particles with 100 A LFCS and symmetric PS potential configuration 47
5.6 Termination of particles with 180 A LFCS setting and symmetric PS potential configuration 47
5.7 Termination of particles with 180 A LFCS setting and asymmetric PS potential configuration 48
5.8 Arrival probability of single electron as a function of the detector ring . . . 50
5.9 Detection probability of clister sizes of 5 calculated and simulated 50
5.10 Detection probability of cluster sizes from 2 to 10 51

6.1 Schematic overview of the cluster detection algorithm 56
6.2 Interarrival times of cluster events coming from tritium β-decays 57
6.3 Interarrival times of cluster events coming from tritium β-decays and uncorrelated background 58
6.4 Uncorrected and corrected cluster size distribution determined with $\Delta t = 0.2\,\mathrm{s}$ 59
6.5 Cluster size distribution of background-free data with $\Delta t = 0.2\,\mathrm{s}$ 59
6.6 Cluster size distribution of background free data with $\Delta t = 4\,\mathrm{s}$ 60
6.7 Cluster size distribution of background free data with $\Delta t = 60\,\mathrm{s}$ 61

7.1 Simulated tracks of positive charged ions through PS without potential . . 68
7.2 Simulated tracks of positive charged ions through the PS with a potential of $-200\,\mathrm{V}$ 69

7.3 Simulation of a single positive ion through PS with a potential of −200 V . 69

List of Tables

5.1 Preparatory simulation - symmetric potential configuration with 100 A LFCS setting 45
5.2 Preparatory simulation - asymmetric potential configuration with 180 A LFCS 48
5.3 Maximum current technical possible for LFCS coils of the MS 49

6.1 Number of cluster detections 61

7.1 Ion currents at the end of the WGTS 67
7.2 LFCS setting for ion tracking simulation 68
7.3 PS potential configuration for ions 70

1. Introduction

The standard model of particles is currently the best developed theory to describe our universe that we know. Part of the standard model are elementary particles such as neutrinos. For a profound understanding of nature, it is important to know the characteristics of each particles, i.e. mass, electric charge and spin. Since the discovery of the neutrino, scientist discussed if it possesses a rest mass or is massless like the photon. With time, neutrino experiments discovered the different flavors of neutrinos. But due to the very small interaction cross-section of neutrinos, the neutrino experiments remained unsuccessful in solving the neutrino mass problem. The confirmation of a non zero rest mass of neutrinos was done by the neutrino experiments at the Sudbury Neutrino Observatory and the Super Kamioka Nucleon decay experiment that observed the neutrino flavor oscillation, which can only be explained by a non zero rest mass of neutrinos.
Until now neutrino mass experiments could only publish upper limits and not the exact mass value and, hence, the exact mass value remains hidden. The motivation of detecting the neutrino rest mass is still up present as it not only expanses the standard model of particles, but also is a primary candidate to solve cosmological issues such as early galaxy formation and dark matter.

The **Ka**rlsruhe **Tri**tium **N**eutrino (KATRIN) experiment aims to probe the mass of the electron antineutrino in a model-independent way with a sensitivity of $m_\nu = 200\,\mathrm{meV/c^2}$ (90% C.L.) by analyzing the β-spectrum of tritium close to the endpoint energy of $E_\mathrm{decay} = 18.6\,\mathrm{keV}$. The β-electrons are generated in the source by tritium β-decay and are guided by a magnetic field through the transport section until they reach the spectrometer, where they are analyzed. However, not only β-electrons are able to enter the spectrometers but also tritium molecules by diffusion processes. A tritium β-decay in the spectrometer section can cause additional background by creating β-electrons that scatter with residual gas, subsequently generating secondary and tertiary electrons. These generated electrons are then able to reach the detector and cause a signal. To suppress this effect, several vacuum pumping-systems are installed to reduce the tritium flux from the source to the spectrometers and, thereby, prevent a tritium contamination of the spectrometers.

In the context of this thesis, the detection sensitivity of tritium β-decays in the pre-spectrometer is investigated on. Knowing the decay rate in the spectrometers allows to check on the functionality of the vacuum pumps (i.e. cryogenic pumps). In short, a feasibility study of checking the functionality of vacuum pumps by counting tritium β-decays in the pre-spectrometer is the main topic of this thesis. Together with preparatory simulations and analysis of the simulation data the feasibility of this method is discussed.
In addition ionized (tritium) molecules are another background source. These ions are not removed by the vacuum pumps efficiently as they are guided by the magnetic fields until they interact with other particles. Preventing them from entering the spectrometers and, hence, avoiding a potential tritium contamination is of great importance.
Neutral and ionized tritium that are able to reach the spectrometer worsen the measurement

data. This thesis deals with understanding their behavior and developing countermeasures to improve the statistics for the measurement of the neutrino mass.

Outline

A general overview of the current understanding of neutrinos is given in chapter 2. Starting with a historical background and current state of the neutrino physics the evidence of the existence of a non-zero neutrino rest mass is given. A mathematical approach of describing the neutrino flavor oscillations which results in a non-zero neutrino rest mass follows after that. The chapter ends with describing different concepts of measuring neutrino masses that can be either model-dependent or model-independent.

Chapter 3 specializes on the KATRIN experimental set up, the measurement principle and the components, from which the beam line consists of.
Since simulation are a major part of this thesis, the used simulation software KASSIOPEIA is explained in chapter 4. The structure of the program and the components of a simulation are described as well as methods of particle tracking and electromagnetic field calculation. The chapter ends with presenting additional implemented functions that were needed in the context of this work.

The investigated background source in terms of trapped particles is described in chapter 5. Apart from that, preparatory simulations are presented that were done to estimate different parameters for the final simulation to save up computing time.

Chapter 6 contains the main part of this thesis and answers the question of the feasibility study. First the simulation and its parameters are explained and discussed. The method of data analysis follows as well as the interpretation of the simulation results. At the end of this chapter, a discussion of the results sums up new insights and presents improvements for future simulations and experiments.

The case for ionized tritium is discussed in chapter 7. The origin of ions and their impact on the measurement results is described as well as a method to minimize their impact on the experiment.

The conclusion together with an outlook in chapter 8 summarizes the results of this work and finishes this thesis.

2. Neutrinos

This chapter focuses on the general theory of neutrinos. Starting with a brief historic overview, the main part of this chapter describes the origin and characteristics of neutrinos and the main motivation for the KATRIN experiment: The non-vanishing neutrino rest mass and its impact on the Standard Model (SM) of particle physics as well as the structure formation in the early universe. The extraordinary nature of these particles that leads many physicists desperate and clueless in the past and even today.

2.1 Historic Background

After the discovery of the β-decay in the early 20^{th} century the emitted β-particles were assumed to have discrete energies as already known from the α-decay. The measured beta energy spectrum of electrons coming from the decay of radium, however, showed an continuous spectrum [1]. When taking energy conservation into account, this could not be explained with only electrons being emitted from β-decays. So in year 1930 Pauli proposed a three-body decay in which in addition to the electron another particle which he named *neutron* is generated, thus, making the β-decay a three-body decay [2]. With two particles being emitted, the continuous energy spectrum of the β-electron could be explained.
The second decay particle should be electrically neutral granting charge conservation and possess spin $\frac{1}{2}$. Pauli also stated a mass of maximal 1 % of the proton mass. In general a β-decay is described as follows

$$ {}^{A}_{Z}\mathbf{X} \longrightarrow {}^{A}_{Z+1}\mathbf{X}' + \underbrace{e^- + \bar{\nu}_e}_{(E_{\text{decay}})} \quad , \tag{2.1} $$

with X as the parent nucleus, X' the emitted daughter nucleus, A the mass number, Z the proton number and a decay energy E_{decay}. After the discovery of the neutron as part of the atomic nucleus by Chadwick in 1932, it was excluded as the sought decay particle due to its mass being too large [3].

Two years later Fermi published his theory of the β-decay as a three-body decay with electrons and neutrinos as the decay particles. The name *neutrino* was given by him and means as much as a tiny version of the priorly found neutron. His mathematical derivation could easily explain the continuous energy spectrum of the β-decay and also postulated a neutrino mass of either zero or much smaller than the electron mass. According to Fermi the β-decay is considered as a perturbation in quantum mechanics, and with *Fermi's Golden Rule* the following model of β-decay was used in his approach

$$ n \longrightarrow p + e^- + \bar{\nu} \quad , $$

with a neutron n decaying into a proton p and the mentioned decay particles (note that at this time the lepton conservation law was still unknown) [4]. Not only did his theory

explain the β^- decay but also the reverse interaction in form of the β^--decay.

With neutrinos having a rather small scattering cross-section with matter the detection of these particles seemed hopeless [5], but 34 years after their postulation C.L. Cowan and F. Reines succeeded in detecting neutrinos for the first time with their experiment called *project poltergeist* in year 1956. Their approach was to detect the following reaction

$$\bar{\nu}_e + p \longrightarrow n + e^+ \quad .$$

Electron antineutrinos coming from a nuclear reactor scatter with protons in a target and produce a neutron and a positron. The positron annihilates with an electron, generating two coincident photons and the neutron emits gamma radiation when it is captured by a nucleus. The target for the electron antineutrinos was a tank filled with water mixed with cadmium. Neutrons coming from the reaction scatter with water molecules and are moderated until they are captured by cadmium. The reactions are

$$e^+ + e^- \longrightarrow \underbrace{\gamma + \gamma}_{(511\,\text{keV each})} \quad , \tag{2.2}$$

$$n + {}^{113}_{48}\mathbf{Cd} \longrightarrow {}^{114}_{48}\mathbf{Cd} + \gamma \quad (\gamma_{tot} = 9\,\text{MeV}) \quad . \tag{2.3}$$

As the neutron takes several milliseconds to be captured, a delayed coincidence measurement of the two γ-signals allows for an effective background discrimination [6].

After the discovery of the electron antineutrino in year 1962 at the *Brookhaven National Laboratory* (BNL) in the United States, L.M. Ledermann, M. Schwartz and J. Steinberger found a different neutrino. A high energy beam of protons with 15 GeV was directed to a beryllium target. In the collision among other particles pions were created [7]. Because of helicity suppression pions rather decay in muons than in electrons, even having an energetic more favorable state for the electron branch [8]. So after the collision of the proton beam with the beryllium target generating pions, one can assume that with a proper shielding (in this case 13.5 m iron wall) a registered signal in a spark chamber behind the shielding wall should be reduced to a neutrino. With knowing that no electrons are produced in the process it is not possible to have electron neutrinos. So the registered signal at BNL should be a neutrino ν_μ that is not equal to ν_e [7].

Having found the third lepton named *tauon* (τ) in year 1975 it was logical to expect a third neutrino type that has yet to be found with the same flavor[9]. It took several years until in year 2000 the DONUT experiment at Fermilab could announce their discovery of the tau neutrino ν_τ. Generation of ν_τ was done with a 800 GeV proton beam colliding with an emulsion target. The created D_S meson decays in a τ lepton and tau antineutrino ν_τ. All other products of the collision were filtered by magnets, concrete, iron and lead shielding so only neutrinos could reach the detector. Tau neutrinos scattered in the detector and generated new τ leptons that were detected to differ between the three neutrino families [10].

Classification of neutrinos

Neutrinos in the SM are categorized as Fermions since they possess halfinteger spins as their lepton partners. Leptons are categorized in three families and six flavors

e^-	μ^-	τ^-
ν_e	ν_μ	ν_τ

with corresponding anti particles having opposite charge, helicity but same spin. Physicists try to go beyond the SM and find more fermion generations with high energy experiments. One experiment probes the decay width of the Z boson. The Z boson can decay in a fermion pair consisting of a neutrino and its charged partner. If there is a fourth generation that is still unknown to us, then the ratio between one decay branch (e.g. $\mu + \nu_\mu$) and all other decay branches should show the number of existing lepton families. To this day there is no statistically significant evidence for a possible fourth generation [8, 11]. But since there are no hints against the existence of a fourth generation the research in this area is part of physics beyond the SM (BSM).

2.2 Neutrino mass

With the discovery of neutrinos many physicists assumed a low mass or even no mass at all for this particle [4, 6]. With experimental data from the Sudbury Neutrino Observatory (SNO) and Super-Kamiokande the question concerning the neutrino mass clarified. In year 2015 T. Kajita and A. McDonald were awarded the Nobel Prize on physics for the discovery of the phenomenon of neutrino oscillations that implies a nonzero neutrino rest mass.

2.2.1 Solar neutrino problem

To describe the fusion processes in stars, scientists came up with a solar model of the sun. This model was expected to deliver knowledge about the age of our local sun and general information on the life time of stars. Major part of the standard solar model (SSM) were fusion reactions which are the source of solar radiation and create amongst other products electron neutrinos [12]. The dominant source of solar neutrinos is the pp-cycle with its net cycle of

$$4\mathrm{p} \longrightarrow {}^4_2\mathbf{He} + 2e^+ + 2\nu_e + 26.73\,\mathrm{MeV} \quad .$$

So overall four protons create a helium atom, two positrons, two electron neutrinos and a decay energy of 26.73 MeV which is distributed to the decay products and accompanying gamma radiation. Other processes that generate neutrinos are displayed in figure 2.1 which gives the full energy spectrum of solar neutrinos. Measuring the neutrino flux coming from the sun therefore provides an experimental test of the SSM. Due to their small interaction cross-section neutrinos are the perfect messenger particles to get information of the solar core.

To prove the solar model right R. Davis launched the chloride-based Homestake-Experiment to measure the neutrino flux coming from the sun. The detection was done trough the reaction

$$\nu_e + {}^{37}_{17}\mathbf{Cl} \longrightarrow {}^{37}_{18}\mathbf{Ar} + e^- \quad . \tag{2.4}$$

The amount of argon atoms found in the chloride target delivered the number of neutrino interaction and with the time frame of the experiment, a flux of neutrinos could be determined. The theoretical neutrino flux coming from the solar model, however, could not be proven as the experimental flux was much lower. Even after calculating the models in a more precise way and checking the experimental set up the outcome did not change

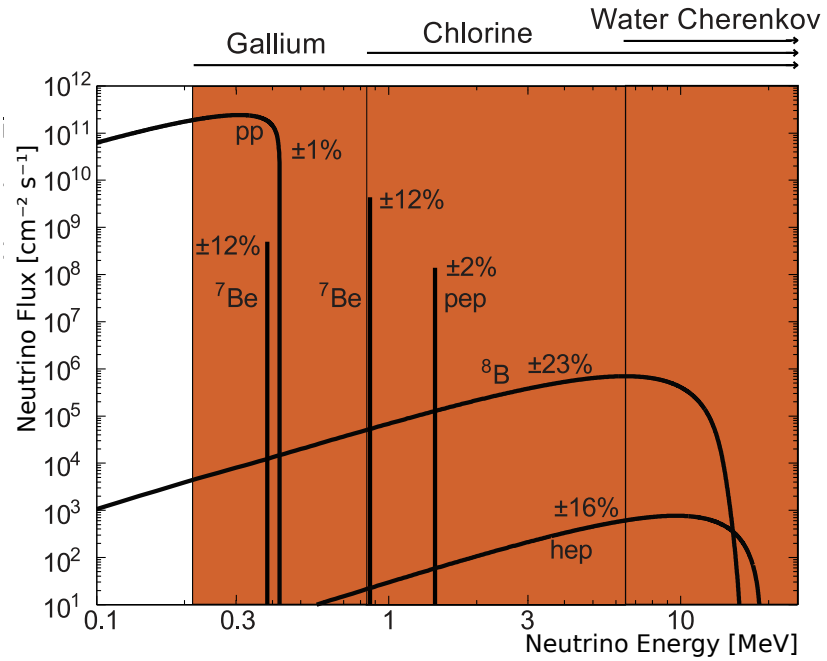

Figure 2.1: Solar neutrino flux generated by different nuclear reactions. The neutrino flux over the neutrino energy is shown for different nuclear reactions. With a total flux of about $2 \cdot 10^{11}\,\mathrm{cm}^{-2}\mathrm{s}^{-1}$ the pp-cycle is the most dominant one. The numbers in percent next to the lines show the theoretical uncertainties of the respective fluxes and the orange colored sections show the elements that are sensitive to the reaction at a certain energy. Adapted from [13].

[14]. So either the SSM was wrong or the experiment itself was not suited for the detection of neutrino fluxes (e.g. the experiment being only sensitive to ν_e and not ν_μ or ν_τ).

To solve the solar neutrino problem a different approach was taken into account. The results of R. Davis and the model calculation of J. Bahcall were considered correct with the addition of neutrinos being able to change their flavor. This happens trough the oscillation between different neutrino states

$$\nu_\alpha \longleftrightarrow \nu_\beta$$

with $\alpha, \beta = (e, \mu, \tau)$. Proof of the existence of neutrino oscillation delivered the Sudbury Neutrino Observatory (SNO) and the Super Kamioka Nucleon Decay Experiment (Super-Kamiokande).

2.2.2 Neutrino oscillation

The idea of neutrino oscillation was first mentioned by B. Pontecorvo. He proposed an effect similar to the meson oscillation between K^0 and $\tilde{\mathrm{K}}^0$ where different quark flavor oscillate to another [15]. Over time, the theory got more attention and received a more sophisticated formulation.

The basic idea of neutrino oscillation like the quark flavor oscillation starts with flavor-eigenstates and mass-eigenstates not being equal. Measured neutrinos are flavor-eigenstates $|\nu_\alpha\rangle$ with $\alpha = (e, \mu, \tau)$ that are a mixture of mass-eigenstates $|\nu_i\rangle$ with $i = (1, 2, 3)$. The question now is how the mass composition of a flavor-eigenstate can be determined. Same as the Cabibbo-Kobayashi-Maskawa-Matrix (CKM-Matrix) for quark-flavor oscillation a

mixing matrix for neutrinos was set up called the Pontecorvo-Maki–Nakagawa–Sakata-Matrix (PMNS-Matrix) [16]. With this unitary 3×3 matrix the mixture of flavor eigenstates can be displayed as

$$|\nu_\alpha\rangle = \sum_i U_{\alpha,i} |\nu_i\rangle \quad , \tag{2.5}$$

with $U_{\alpha,i}$ from

$$U_{PMNS} = \begin{pmatrix} U_{e,1} & U_{e,2} & U_{e,3} \\ U_{\mu,1} & U_{\mu,2} & U_{\mu,3} \\ U_{\tau,1} & U_{\tau,2} & U_{\tau,3} \end{pmatrix} \quad . \tag{2.6}$$

The parametrization of the PMNS-Matrix uses three mixing angles θ_{12}, θ_{13}, θ_{23} and one CP violating (charge-parity) phase δ

$$U = \begin{pmatrix} c_{12}c_{13} & s_{12}c_{13} & s_{13}e^{-i\delta} \\ -c_{23}s_{12} - s_{23}c_{12}s_{13}e^{i\delta} & c_{23}c_{12} - s_{23}s_{12}s_{13}e^{i\delta} & s_{23}c_{13} \\ s_{23}s_{12} - c_{23}c_{12}s_{13}e^{i\delta} & -s_{23}c_{12} - c_{23}s_{12}s_{13}e^{i\delta} & c_{23}c_{13} \end{pmatrix} \quad , \tag{2.7}$$

with $s_{ij} = \sin\theta_{ij}$ and $c_{ij} = \cos\theta_{ij}$ [17]. The mass eigenstates in equation 2.5 can be seen as stationary eigenstates of the Hamilton operator H with eigenvalue E. Neutrinos are in a pure flavor eigenstate in the moment they are produced. For the production at $t = 0$ the mass eigenstate of the neutrino can be described as a plane wave that is a solution of the Schrödinger's Equation)

$$|\nu_i(t)\rangle = e^{-E_i t} |\nu_i\rangle \quad . \tag{2.8}$$

For $t > 0$ the neutrino is a mixture of mass eigenstates described as

$$|\nu_\alpha(t)\rangle = \sum_i U_{\alpha i} e^{-iE_i t} |\nu_i\rangle \quad . \tag{2.9}$$

Using equation 2.5 shows a relation of two flavor eigenstates

$$|\nu_\alpha(t)\rangle = \sum_{i,\beta} U_{\alpha i} U^*_{\beta i} e^{-iE_i t} |\nu_\beta\rangle \quad . \tag{2.10}$$

The probability of ν_α oscillating to ν_β is derived via

$$P_{\nu_\alpha\to\nu_\beta}(t) = |\langle\nu_\beta(t)\nu_\alpha(t)\rangle|^2 = \sum_{i,j} U^*_{\alpha,i} U_{\beta,i} U_{\alpha,j} U^*_{\beta,j} e^{-i(E_i - E_j)t} \tag{2.11}$$

and for the ultra-relativistic case where $p_i \gg M_i$ and $E \approx p_i$ applies, it follows

$$P_{\nu_\alpha\to\nu_\beta}(L/E) = \sum_{i,j} U^*_{\alpha,i} U_{\beta,i} U_{\alpha,j} U^*_{\beta,j} e^{-i\frac{\Delta m^2_{ij} L}{2E}} \quad , \tag{2.12}$$

with distance L between neutrino location at $t = 0$ and detector and energy E of the neutrino. Note that $\Delta m^2_{ij} \equiv m^2_i - m^2_j$ and can in fact be negative. To measure neutrino

oscillation in the most effective way one has not only to consider the mixing angles coming from the PMNS-matrix but also the distance of neutrino source to the detector, the energy and the mass difference. *Long baseline experiments* generate neutrinos with accelerators or reactors and place a detector at a specific distance L that is optimized to scan a certain Δm and θ_{ij}-range.

To sum it up, neutrinos must have a non-vanishing rest mass to explain the phenomenon of neutrino flavors oscillations. In reverse, neutrino oscillation can be seen as an irrevocable evidence for neutrinos to possess a rest mass.

2.2.3 Neutrino oscillation experiments

Several neutrino experiments try to probe the mixing ratio of the flavor eigenstates. For this intention one has to determine the mixing angles θ_{ij} as mentioned above in the parametrized PMNS-matrix 2.7. While experiments like SNO and Super-Kamiokande use Cherenkov radiation to detect neutrinos, other experiments like the Gallium-Experiment (GALLEX) have a similar detection method as the Homestake experiment by using nuclear reactions [18, 19, 20].
Recent results of neutrino experiments show non-vanishing values for the mixing angles and mass differences of the mass eigenstates. There are two popular theories that are in agreement with current experimental data. Firstly

$$m_1 < m_2 \ll m_3 \tag{2.13}$$

is called the normal neutrino mass hierarchy and secondly

$$m_3 \ll m_1 < m_1 \tag{2.14}$$

is called the inverted mass hierarchy [21].

In figure 2.2 both mass hierarchies are displayed with their assumed mass differences. The figure also shows the mixing ratio of flavor eigenstate making up a mass eigenstate. This is a simple reversal of equation 2.5 to

$$|\nu_i\rangle = \sum_i U^*_{\alpha,i} \, |\nu_\alpha\rangle \quad . \tag{2.15}$$

The value of m_3 can not be determined with the results achieved so far. For a decent model of a neutrino mass hierarchy it is not sufficient to know the mass differences but of utmost importance to know the absolute neutrino masses. So in the end it all comes down to measuring the neutrino rest mass with a decent method allowing little uncertainties.

2.3 Measuring the neutrino mass

Neutrino oscillation experiments like SNO or Super-Kamiokande are only sensitive to the mass difference of neutrino mass eigenstates and can not measure the rest mass itself. For this task other experimental methods have to be considered. The direct approach of measuring neutrino mass is model-independent (e.g. investigating β-decay by kinematic means). Experiments that need theoretical additions for their parameters can be categorized as model-dependent experiments.

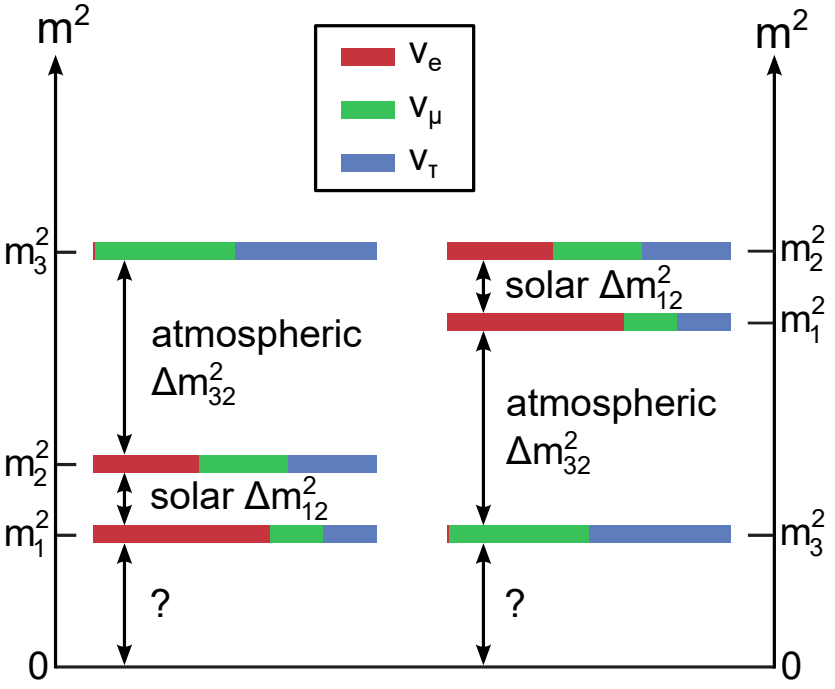

Figure 2.2: Normal and inverted neutrino mass hierarchy. Neutrino mass eigenstates are shown as a mixture of flavor eigenstates with different proportions. Every flavor eigenstate is a non-vanishing part of the mass eigenstate. The left side shows mass differences on the normal hierarchy, while the right side shows the inverted neutrino mass hierarchy. With the experimental results so far it is not possible to determine whether m_3 is heavier or lighter than the other two mass eigenstates. Adapted from [22].

2.3.1 Neutrinos in cosmology

In the early years of the universe neutrinos of each flavor were generated at high energies in a state of thermal equilibrium. As the universe expanded further on, interaction of neutrinos with the surrounding baryonic mass became inefficient due to the weak interaction rate being smaller than the expansion rate of the universe. Those *relic neutrinos* stopped interacting with the surrounding plasma resulting in the cosmic neutrino background. This process is called *neutrino decoupling* analog to the generation of the cosmic microwave background due to photon decoupling [23].
Relic neutrinos have not been detected yet because of their low energies and rather small cross-sections. Cosmological models, however, deliver a prediction of the density of the cosmic neutrino background of $\Omega_\nu = 339\,\mathrm{cm}^{-3}$ which can be used to calculate a model-dependent neutrino mass of

$$\sum_i m_i = 93\Omega_\nu h^2\,\mathrm{eV} \tag{2.16}$$

with h as the dimensionless Hubble parameter. Using this model the Planck satellite was able to set an upper limit on the sum of all neutrino masses of

$$\sum_i m_i = 0.23\,\mathrm{eV} \tag{2.17}$$

at 95% confidence level [24]. Being heavily model-dependent this results should be viewed with caution.

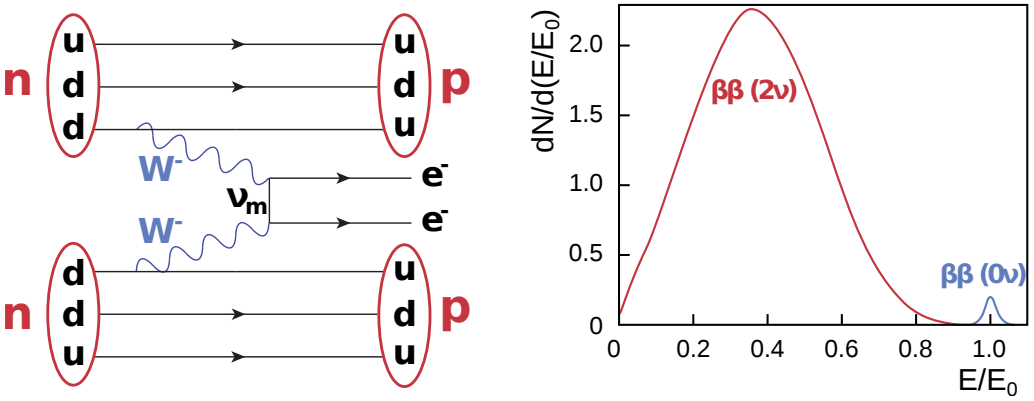

Figure 2.3: Left: Feyman diagram of the neutrinoless double beta decay. The Feynman diagram shows two neutrons of a parent nucleus decaying at the same time into two protons and two electrons via virtual Majorana neutrinos that annihilate with each other. Adapted from [26]. **Right: Energy spectrum of the double β-decay with two emitted neutrinos (red) and of the neutrinoless double β-decay without neutrino emission (blue).** The energy spectrum for the neutrinoless $0\nu\beta\beta$ decay has a clean peak at the decay energy. The $2\nu\beta\beta$ decay has a continuous energy spectrum. Adapted from[27, 28].

2.3.2 Neutrinos from supernovae

In supernovae[1] models a large part of the energy is radiated off in form of neutrinos. The time t_0 for those neutrinos to reach the earth depends on their energy E_ν and mass m_ν. As E_ν depends also on m_ν two neutrinos have to be observed and evaluated together with different times t_0 and t_1. The distance of supernovae can be determined with different astronomic methods that deliver a value for t_0 but is model-dependent as the generation of neutrinos is a phase in a supernova collapse that is only theoretically described. With the time difference of both signals $\Delta t = t_0 - t_1$ it is possible to calculate a neutrino mass [25].

2.3.3 Neutrinoless double β-decay

The neutrinoless double β decay ($0\nu\beta\beta$) is a theoretical decay of a parent nucleus which performs two β decays simultaneously with no neutrinos emitted. This kind of reaction is possible when neutrinos are Majorana-like particles which means that a neutrino is its own anti particle. Figure 2.3 illustrates the Feynman diagram at a $0\nu\beta\beta$ decay and the energy spectrum of the standard double β-decay with two emitted neutrinos ($2\nu\beta\beta$) and the $0\nu\beta\beta$ decay.

Some isotopes are able to decay in rare cases through $2\nu\beta\beta$ if the single β-decay is energetically forbidden. The decay is either β^-

$$2n \longrightarrow 2p + 2e^+ + 2\nu_e \quad , \tag{2.18}$$

or β^+

$$2p \longrightarrow 2n + 2e^- + 2\bar{\nu}_e \quad . \tag{2.19}$$

Until now no $0\nu\beta\beta$ decay has been detected. However experiments like the Germanium Detector Array (GERDA) try to achieve this goal [29]. If detected, the $0\nu\beta\beta$ decay would

[1] a supernova is a collapsing star at the end of its lifetime

not only prove neutrinos being Majorana-like particles but also allow to calculate the neutrino mass. The half life of an isotope performing $0\nu\beta\beta$ depends on the neutrino mass

$$[T^{0\nu}_{1/2}(0^+ \to 0^+)]^{-1} = G^{0\nu}(E_0, Z) \left| M^{0\nu}_{GT} - \frac{g_V^2}{g_A^2} M^{0\nu}_F \right|^2 \langle m_{\nu\beta\beta} \rangle^2 \tag{2.20}$$

with

- $G^{0\nu}(E_0, Z)$ as the phase space integral,
- $M^{0\nu}_{GT}$ as the model dependent Gamov-Teller matrix element,
- $M^{0\nu}_F$ as the model dependent Fermi matrix element,
- g_V/g_A as the axial and vector coupling constant and
- $m_{\nu\beta\beta}$ as the effective neutrino mass which is $\langle m_{\nu\beta\beta} \rangle^2 = \left| \sum_{i=1}^{3} U_{ei} m_i \right|^2$ [30].

Equation 2.20 is valid if the $0\nu\beta\beta$ decay is mediated by the exchange of light neutrinos that are model dependent Majorana-particles. Recent experimental results could only limit the half time, setting an upper limit to the neutrino mass of [29]

$$m_{\nu\beta\beta} < 0.2 - 0.4\,\text{eV} \quad . \tag{2.21}$$

2.3.4 Neutrino mass from single β-decay

Another method of measuring the neutrino mass is to analyze the energy spectrum of an atom performing β-decay. The left side of figure 2.4 illustrates the Feynman-diagram of the β^--decay. A neutron emits a W^- boson that decays into an electron and an electron antineutrino. The energy spectrum of the β-electrons on the right side of figure 2.4 shows two cases, one for a neutrino mass equal to 1 eV and one equal to zero. Close to the endpoint energy E_0 of the spectrum the neutrino mass has an input on the spectral shape. For a neutrino mass equal to zero (red line in figure 2.4) the endpoint energy of the spectrum is equal to the theoretical endpoint energy of the decay, which means emitted electrons of a β decay can reach the maximum amount of released energy. If the neutrino mass is nonzero (blue dashed line in figure 2.4), then the maximum energy reachable for the electrons is the endpoint energy E_0 minus the mass of neutrinos m_ν.

The main task of a neutrino mass experiment that analyzes the β^--electron spectrum is to investigate the endpoint region of the spectrum. Here, the measured energy spectrum does not reach the theoretical endpoint energy but a maximum energy of $E_0' = E_0 - E_\nu$. With this difference it is possible to calculate the neutrino mass via

$$E_\nu = E_0 - E_0' = m_\nu c^2. \tag{2.22}$$

The Karlsruhe Tritium Neutrino Experiment is the latest of a series of direct neutrino mass experiments probing the mass of the electron antineutrino by analyzing the energy spectrum of electrons coming from tritium β^--decay. This decay has an endpoint energy of $E_0 = 18.6\,\text{keV}$ and is given by

$${}^3_1\mathbf{H} \longrightarrow {}^3_2\mathbf{He} + \underbrace{e^- + \bar{\nu}_e}_{18.6\,\text{keV}} \quad . \tag{2.23}$$

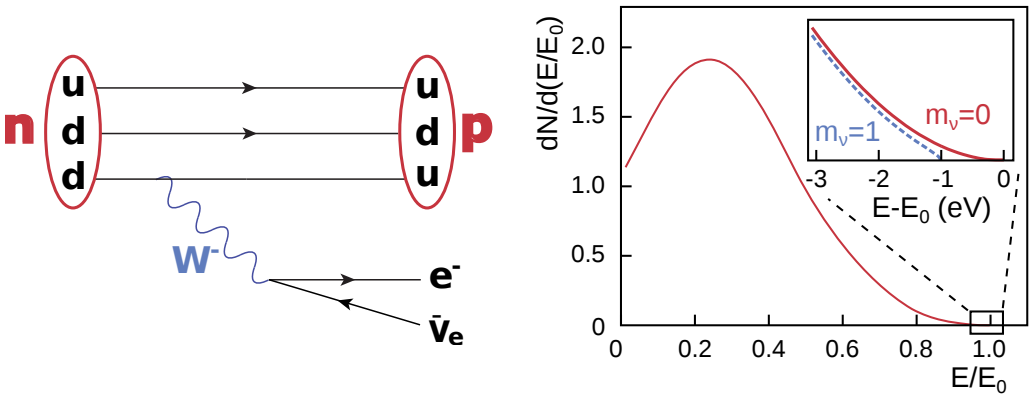

Figure 2.4: Left: Feyman diagram of the single β^--decay. The Feynman diagram shows the β^--decay mediated by the exchange of a W^- boson resulting in an electron and an electron antineutrino. Figure adapted from [26]. **Right: Energy spectrum of electrons from a β^--decay.** The energy spectrum shows two cases for the neutrino mass. Red line implies a neutrino mass equal to zero and the blue dashed line implies a neutrino mass equal to 1 eV. Measuring the difference of maximal energy of electrons and endpoint energy E_0 leads back to the neutrino mass of the electron antineutrino $\bar{\nu}_e$. Figure adapted from [27].

A more detailed description of this experiment regarding tritium source, filtering and analysis principle is given in chapter 3.

In theory the β-decay is described by Fermi's Golden rule as a transition of an initial state $|i\rangle$ to a final state $|f\rangle$

$$\Gamma_{i\to f} = 2\pi \cdot |M_{fi}|^2 \rho(E_f) \quad , \tag{2.24}$$

with the transition rate $\Gamma_{i\to f}$ describing the transition $i \to f$, M_{fi} being the transition matrix element and $\rho(E_f)$ giving the density of final energy states. Integrating over all possible states the energy spectrum of the β-decay can be derived from 2.24 to

$$\frac{\mathrm{d}^2 N}{\mathrm{d}E\mathrm{d}t} = \frac{G_F^2 \cos^2\Theta_C}{2\pi^3 c^5 \hbar^7} \cdot M \cdot F(E, Z{+}1) \cdot p_e \cdot (m_e c^2 {+} E) \cdot (E_0 {-} E) \cdot \sqrt{(E_0 - E) - m_{\nu_e}^2 c^4} \quad . \tag{2.25}$$

Here G_F is the Fermi coupling constant, Θ_C the Cabibbo angle, M the nuclear matrix element, $F(E, Z+1)$ the Fermi function, E_0 the endpoint energy and p_e, m_e and E are the momentum, mass and energy of the emitted β-electron [31].

As the theory of this experimental method is well known, it manages to be completely independent of any advanced theoretical models, making the KATRIN experiment perfectly suited to probe the mass of neutrinos.

3. KATRIN

The KATRIN experiment aims to probe the mass of the electron antineutrino $\bar{\nu}_e$ with a sensitivity of $200\,\mathrm{meV/c^2}$ (90% C.L.) by analyzing the energy spectrum of tritium β-decay. Located at the Karlsruhe Institute of Technology (KIT) the experiment profits from the extensive infrastructure and the expertise of the Tritium Laboratory Karlsruhe (TLK) which is located on site and has the license to handle 40 g of gaseous tritium.
This chapter describes the measurement method of the experiment which is based on the *Magnetic Adiabatic Collimation combined with an Electrostatic Filter* (MAC-E) principle and gives an overview of the 70 m long beamline of the experiment including the tritium source, a transport section, spectrometers and the detector section.

3.1 Measurement Principle

As mentioned in chapter 2 the main task of KATRIN is to analyze the energy spectrum of β-electrons coming from tritium β-decay close to the endpoint energy 18.6 keV. For this purpose it uses an electrostatic potential spectrometer where the signal electrons with kinetic energy

$$E_{\mathrm{kin}} = E_{\mathrm{kin}}^{\parallel} + E_{\mathrm{kin}}^{\perp} \tag{3.1}$$

have to overcome a retardation potential of $E_{\mathrm{el}} = qU_0$ to be counted by a detector. By varying the retardation voltage U_0 of the spectrometer by different potentials $\delta U \propto \delta E_{\mathrm{el}}$ the integral β-spectrum close to the endpoint energy is measured.

Electrons generated by β-decay, however, are emitted isotropically. Thus, only a small fraction of electrons are emitted such that their full kinetic energy $E_{\mathrm{kin}} = E_{\mathrm{kin}}^{\parallel}$ is analyzed by the retardation potential. In order to use the full luminosity of the source, the momentum of all other electrons must be collimated when approaching the point of maximum potential U_0. For this purpose KATRIN uses the well-established MAC-E filter principle principle.

3.2 The MAC-E filter

The MAC-E concept allows for high energy resolutions while still using most of the source luminosity. It is based on the magnetic bottle/mirror effect where charged particles change their direction of momentum in an inhomogeneous magnetic field.

Charged particles are guided by the magnetic field and follow the field lines in a cyclotron motion. The magnetic moment of a particle in first order (without considering relativistic effects) given by

$$\mu = \frac{E_{\perp}}{B} \tag{3.2}$$

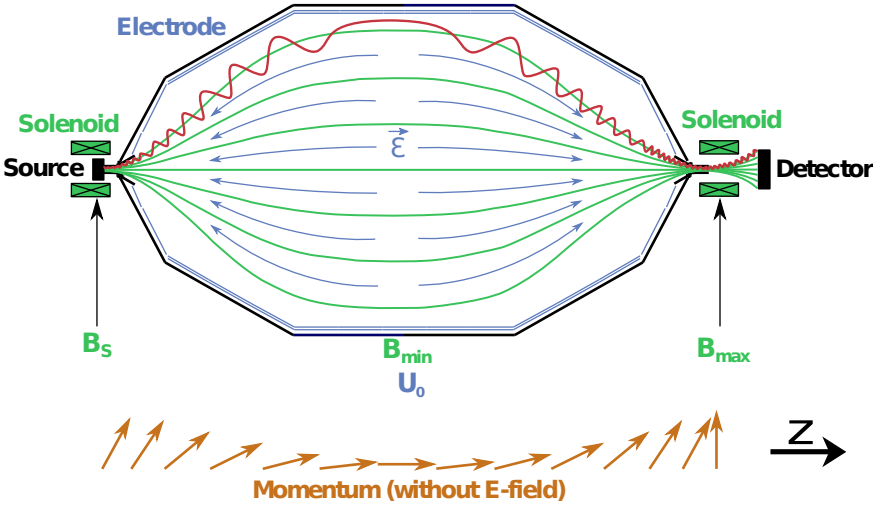

Figure 3.1: MAC-E filter principle. Particles from the β-source fly on cyclotron trajectories (red line) along the magnetic field line (green line). While a decrease of $\vec{B}$ leads to a decrease of $E_{\text{kin}}^{\perp}$ and, thus, an increase of $E_{\text{kin}}^{\parallel}$ resulting in a collimation of the electron momentum relative to the field line. A requirement of this effect is for the magnetic field to decrease/increase slowly granting adiabatic movement. Particles with enough energy can overcome the electrostatic potential qU_0 and reach the detector. Figure adapted from[32].

is conserved if the movement of the particle is adiabatic. In an inhomogeneous magnetic field this is the case when the decrease (increase) of $B_{\text{max}} \xrightarrow{(\leftarrow)} B_{\text{min}}$ happens slow enough, i.e. if it is guaranteed that the particle follows the same magnetic field line at all times. In this case, a decreasing magnetic field leads to a decrease of $E_{\text{kin}}^{\perp}$ in equation 3.2. Due to conservation of kinetic energy, however, a decrease of $E_{\text{kin}}^{\perp}$ results in an increase of $E_{\text{kin}}^{\parallel}$ and thus, in a collimation of the electrons momentum in the direction of flight.

Figure 3.1 gives an overview of the working principle of a MAC-E filter. Being emitted isotropically in the source the particle is guided on a cyclotron trajectory into the spectrometer where it undergoes magnetic adiabatic collimation. The collimation of the momentum is indicated by arrows below the plot (considering the electric field would change the size of the arrows). Behind the analyzing plane where the magnetic field is increasing again, the particle shifts its angle of momentum back into its original direction. The momentum angle turning back does not matter anymore at this point as the particle's energy is already analyzed and it will now be counted by the detector.

3.2.1 Trapped particles

As such a MAC-E filter represents a magnetic bottle there is the possibility for particles to be trapped between magnetic mirrors. When particles fly along an increasing magnetic field their transversal energy increases as stated by equation 3.1 and 3.2. Under a certain condition for the entrance angle of the particle it can be reflected before reaching the detector side. A maximum angle of the electron direction with respect to the B-field line can be derived that allows the particle to still reach the detector as

$$\theta_{max} = \arcsin\left(\sqrt{\frac{B_{\text{max}}}{B_{\text{min}}}}\right) \quad . \tag{3.3}$$

Using more complex configurations of electric potentials can cause Penning traps to occur. A Penning trap limits the movement of charged particle at two ends with electrostatic

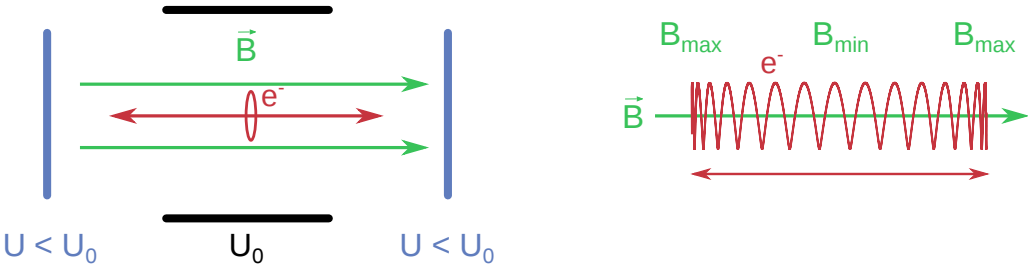

Figure 3.2: Penning trap and magnetic-bottle trap. Left: A charged particle with a low kinetic energy can not overcome the electrostatic potential at both sides and is trapped. **Right:** A charged particle is reflected at both ends by the magnetic mirror effect. Figure from [33].

potentials that have higher energy than the kinetic energy of the trapped particle. While the particle is radially trapped by the B-field, figure 3.2 shows on the left side a trapped particle that does not have enough energy to overcome the potential barrier at both ends and ends up being trapped in between. On the right side of figure 3.2, a charged particle is reflected at both ends by the magnetic mirror effect and can not leave the trap. A similar effect to the magnetic bottle/mirror can be observed in the nature as the Van Allen radiation belt. The magnetic field of the earth causes a magnetic bottle in which particles from the solar wind are trapped and reflected at its ends ending up as polar lights when interacting with the earth atmosphere.

3.2.2 Energy resolution and conservation of the magnetic flux

The energy resolution of the spectrometer is linked to the course of the magnetic field. Since $B_{min} > 0$ applies to all experimental scenarios (as it is needed to proper guide the particles), the charged particle flying across the spectrometer will still keep a fraction of its transverse kinetic energy $E_\perp$. The worst case scenario is a particle with only transversal kinetic energy $E_{\text{kin}} = E_{\text{kin}}^{\perp}$ at the point of maximum magnetic field B_{max}. With this an energy resolution (filtering width of the MAC-E filter) can be derived from equation 3.2 to

$$\Delta E = \frac{B_{\text{min}}}{B_{\text{max}}} \cdot E_{\text{kin}} \quad . \tag{3.4}$$

The magnetic flux Φ is defined by the area A that encloses a magnetic field $\vec{B}$ and is conserved. The formula is given by

$$\Phi = \int_A \vec{B} \cdot \mathrm{d}\vec{A} = \text{const.} \quad . \tag{3.5}$$

For the case of a homogeneous magnetic field and a circular area the flux can be simplified to

$$\Phi = B \cdot A = 2\pi r^2 \cdot B = \text{const.} \quad . \tag{3.6}$$

An increase of the magnetic field results in a decrease of the radius of the area of the *flux tube* and vice versa. One benefit of considering the flux is, that particle starting in a certain flux tube will stay in that flux tube (with adiabatic motion), thus, making it possible to limit an area that is interesting for the experiment.

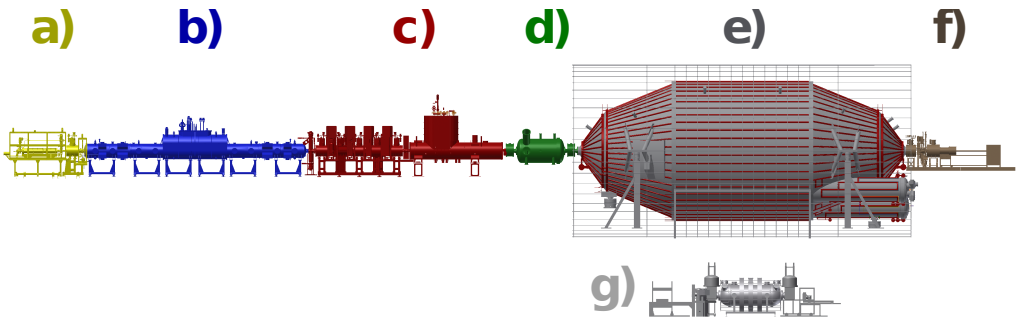

Figure 3.3: The experimental setup of KATRIN consists of seven main components: **(a)** The rear section is used for monitoring and calibration of the source. **(b)** The windowless gaseous tritium source provides the signal electrons coming from tritium β-decay. **(c)** The transport section guides the electrons adiabatically while reducing the tritium flux from the source by 14 orders of magnitude. **(d)** The pre-spectrometer acts as a pre-filter for low-energy electrons. **(e)** The main-spectrometer analyzes the β-spectrum near the endpoint energy. **(f)** The detector counts the electrons that passed the MS and is responsible for data acquisition. **(f)** The monitor spectrometer monitors the stability of the retarding potential of the main-spectrometer. Figure adapted from [34].

The needed conservation of the magnetic momentum in equation 3.2 and the energy resolution in equation 3.4 are the reason why the main-spectrometer of KATRIN has the dimension that it has now.

3.3 KATRIN beamline

The complete KATRIN beamline starts in the **T**ritium **L**abor **K**arlsruhe (TLK) with the rear section and the *Windowless Gaseous Tritium Source* (WGTS). After the WGTS the transport section follows up containing the *Differential Pumping Section* (DPS) and the *Cryogenic Pumping Section* (CPS). At the end of the beamline in the *Spectrometer and Detector Section* (SDS) the *pre-spectrometer* (PS), the *main-spectrometer* (MS) and the *focal-plane detector* (FPD) are located. The monitor spectrometer is used for monitoring purposes regarding the stability of the retarding potential of the main-spectrometer. Figure 3.3 shows the full experimental setup of KATRIN.

3.3.1 The rear section

The rear section is needed for calibration measurements and monitoring of the tritium source activity. For this purpose it uses the fact that half of the electrons coming from the WGTS will be guided towards the rear section. As β-decay leaves behind positive tritium ions a space charge can build up in the source. But having the possibility of space charges in the WGTS requires a possibility to define the electric potential in the source. This is done by a rear plate of a well-defined electric potential [35]. An electron gun housed in the rear section allows the measurement of the column density in the tritium source [36].

3.3.2 The WGTS

The WGTS consists a 10 m long source tube with a diameter of 90 mm which is housed in a complex source cryostat. The column density in the beam tube is stabilized on a 10^{-3} level at $\rho d = 5 \cdot 10^{17}\,\mathrm{cm}^{-2}$. This corresponds to a source activity of $A \simeq 10^{11}\,\mathrm{Bq}$. To reduce distortions of the signal electron energies due to thermal Doppler broadening the beam tube is cooled to 30 K by a novel two-phase neon cooling concept reaching a temperature stability of 3 mK. While tritium is pumped out on both sides of the source tube via turbo-molecular pumps, a series of superconducting solenoids provides a guiding magnetic field of $B_S = 3.6\,\mathrm{T}$ to ensure an adiabatic transport of the signal electrons in a $191\,\mathrm{Tcm}^2$ flux tube towards the spectrometers [35].

3.3.3 The transport section with DPS and CPS

The transport pumping section consists of two pumping systems, the differential pumping section (DPS) and the cryogenic pumping section (CPS) which reduce the flow of tritium from the source towards the spectrometer by 14 orders of magnitude. At the same time superconducting solenoids provide a magnetic field that guides the β-electrons adiabatically to the spectrometers. The DPS consists of six turbo-molecular pumps that reduce the flow of $\mathbf{T}_2$ by a factor of 10^5. Two of the five beam tubes of the DPS are tilted by 20° creating a chicane to increase the pumping efficiency of the turbo-molecular pumps which are located in between the beam tubes [35]. Besides neutral molecules there also exist ions that have to be blocked on their way to the spectrometers. Negative ions can be blocked by a more negative potential at the PS. Positive charged ions are blocked by two ring electrodes in the transport section with a potential of +100 V each. The positive potential should not have an impact on signal electrons with energies higher than 18 keV (see chapter 7). The detection of the ions is done by a Faraday cup [37].

The subsequent CPS uses cryosorption to bind the tritium gas on its 3 K cold which is covered by an argon frost layer. With this the $\mathbf{T}_2$ flow can be further reduced by a factor of 10^7. In regular intervals of three months the CPS must be regenerated by warming it up to 100 K flushing it with gaseous helium, cooling it down again and preparing a new argon frost layer. Similar to the DPS the CPS has two 20° chicanes preventing a direct line of sight to the PS and, therefore, improving the efficiency of the cryogenic pump [35].

3.3.4 Spectrometer and detector section

At the downstream end of the CPS the pre-spectrometer is located. This MAC-E filter spectrometer is based on a cylindrical tank with a length of 3.38 m and an inner diameter of 1.68 m. In the past it served as a prototype for the MS and was used „to verify the extreme high vacuum, testing the reliable operation of heating/cooling system and investigating the performance and properties of the new electro-magnetic design“[35]. For later operation of KATRIN the PS is meant to pre-filter low energy β-electrons reducing their incoming flux from $10^{10}\,\mathrm{s}^{-1}$ to $10^{4}\,\mathrm{s}^{-1}$ in the MS. The electrode system of the spectrometer is made up by a hull electrode, wire electrodes, two full-metal electrodes on both ends and two ground electrodes, also on both ends. The full-metal electrode facing the CPS is called the upstream full-metal electrode, the one facing the main-spectrometer is called the downstream full-metal electrode. The electrostatic potential set up by the hull electrode is smoothed by the wire electrodes and the full-metal electrodes. Figure 3.4 shows the inner electrodes of the pre-spectrometer. There are two superconducting coils at the ends of the PS called PS1 (upstream) and PS2 (downstream) and are operated at a magnetic field of $B = 4.5\,\mathrm{T}$ [35].

The MS is a bigger version of the PS. With a length of 23.3 m and an inner diameter of 9.8 m it meets the requirement of the targeted energy resolution (see section 3.2). The hull of the spectrometer itself is an electrode to set up a starting potential. Fine tuning can be achieved by modifying the potential offset of individual wire electrodes. Two conical ground electrodes mark the beginning and the end of the MS. In addition to the superconducting solenoids on both sides of the spectrometer for the adiabatic guidance of the particles the MS possesses 14 air coils (LFCS) that allow to fine shape the flux tube in the spectrometer and an earth magnetic field compensation system (EMCS) which compensates the earth's magnetic field. The highly desired energy resolution of $\Delta E = 0.93\,\mathrm{eV}$ can be achieved by a homogeneous electric retarding potential and magnetic field in the analyzing plane (where $B = B_{\mathrm{min}}$). The pinch magnet at the downstream side (facing the detector) provides a maximum magnetic field of $B_{\mathrm{pinch}} = 6\,\mathrm{T}$. By setting B_{pinch} with $\frac{B_{\mathrm{S}}}{B_{\mathrm{max}}}$, a maximum

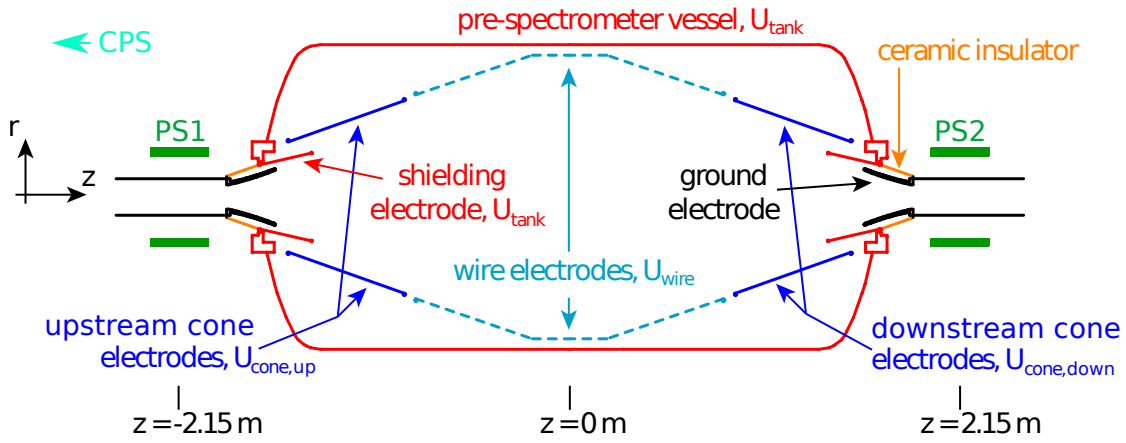

Figure 3.4: Position and geometry of electrodes in the PS. . Figure adapted from [38].

starting angle $\theta_{max} = 51°$ for the β-electrons in the WGTS is set and the accepted area is $A_S = 53\,\mathrm{cm}^2$, which represents a flux of $\Phi = 191\,\mathrm{Tcm}^2$ [35].

Particles that succeeded in overcoming the prior mentioned potentials impinge on the focal-plane detector wafer. The wafer itself is a silicon pixel detector with a circular surface and a diameter of 90 mm (see figure 3.5). The wafer is divided into twelve rings that surround the center of the detector called the *bulls eye* and are numbered from 0 (bulls eye) to 12 (outermost ring). The bulls eye is made up by four pixels and the twelve outer rings are divided into twelve pixels each. Altogether there are 148 pixels on the focal-plane detector. Wafer pixels are silicon diodes that and need a bias voltage which is supplied by the bias ring. The guard ring protects the outer ring pixels by minimizing field distortions from the the bias ring. The outermost ring, however, is not supposed to measure any signal as the magnetic flux at this radius exceeds the design value of $\Phi = 191\,\mathrm{Tcm}^2$.

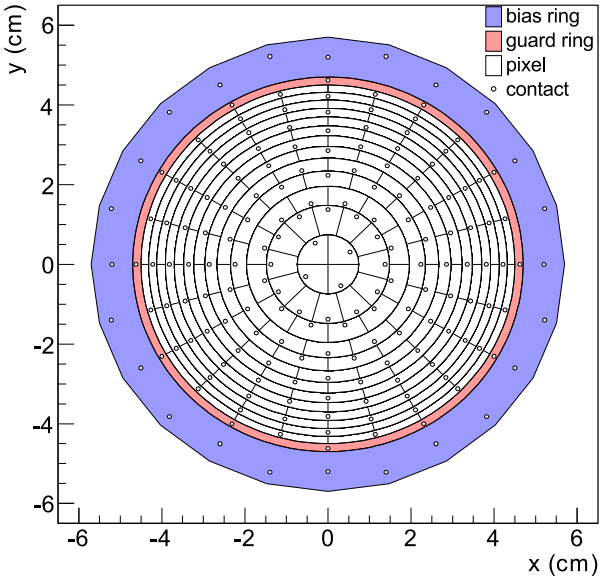

Figure 3.5: Schematic overview of the layout of the KATRIN detector wafer. The wafer is divided into 12 rings with 12 pixels on each ring. The center of the detector is called the *bulls eye* and has four pixels. Altogether there are 148 pixels on the wafer. The bias ring supplies the silicon wafer with bias voltage and the guard ring protects the wafer from potential disturbances. Figure adapted from [39].

4. Simulations with KASSIOPEIA

Recently physics experiments have become larger and more expensive as modern theories tend to go to higher energies and/or higher precisions. A large experiment like KATRIN needs theoretical data in order to reduce unnecessary costs and allow an effective usage of time which is important for the experiments. In addition to that, simulations and theoretical models allow physicists full control over the experiments resulting in a more likely success. The KATRIN collaboration developed its own particle tracking program named KASSIOPEIA. The KASSIOPEIA code is written in C++ and allows the user to track particles in self-defined boundary conditions like geometries or electromagnetic fields. The object oriented code enables the user to further expand the code. The compiled code possesses many input parameters that are gathered in XML-files (Extensible Markup Language). The script language XML allows a user-friendly interface to configure the simulation. A simulation with KASSIOPEIA starts with reading the input from the XML-file and checking if all needed parameters are defined. If no errors occur, the program starts with the particle generation, continues with the tracking and finishes when all particles are terminated. All these parameters have to be set by the user beforehand.
This chapter focuses on the simulation program itself including particle generation, tracking and termination. Information about the outer structure of the simulation code and the framework KASPER in detail can be found in the doctoral thesis of S. Groh [40].

4.1 Starting a simulation

A simulation consists of many configuration settings, like geometries, potentials and solenoid currents that are written in a XML-file. Geometries define the component structure of the simulation. In case of KATRIN, the whole beamline containing the spectrometers, magnetic coils and all the other components make up the basic geometry.

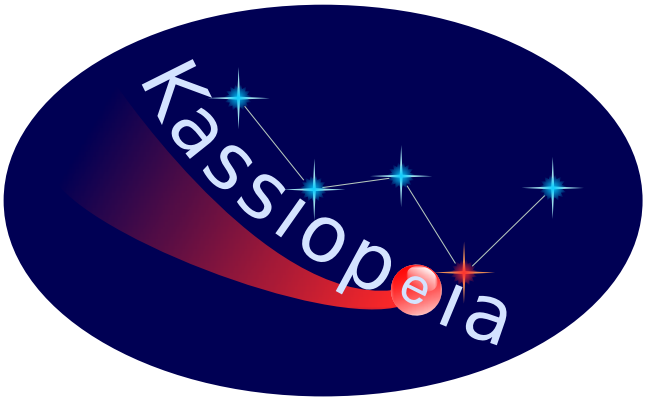

Figure 4.1: The logo of the KASSIOPEIA program. Figure from [40].

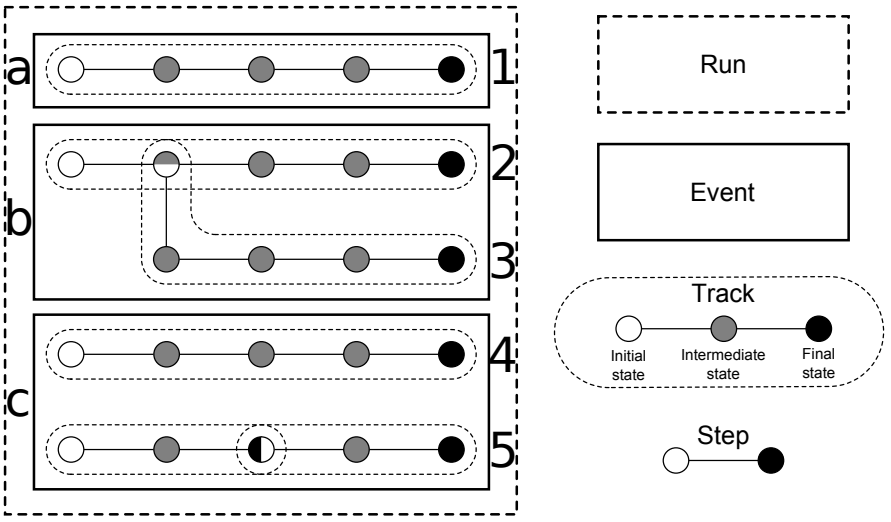

Figure 4.2: KASSIOPEIA simulation structure. The dashed box displays a run containing three events. The three boxes with solid lines are the events **(a)**, **(b)** and **(c)** that are made up by the tracks **(1)** - **(5)** (track number **(5)** turns into track number **(6)**). Track **(1)** is a particle that is generated and terminated after four steps. In event **(b)**, the first track splits up in two tracks which is possible with interactions, like decays or scatterings. Both tracks have to be terminated to finish the event. Track **(5)** is a particle that is terminated by creating another particle and as a result, another track (track **(6)**) occurs. Figure adapted from [40].

4.1.1 Structure of a simulation process

A simulation process has a defined hierarchy. The highest level of hierarchy is called *run*. These runs are made up by *events* which again contain *tracks*. Each track has an initial state and a final state of a particle. The track of a particle consists of *steps* that show the progress of a track (particle) during the simulation. Basically, the hierarchy reads as follows

$$run \rightarrow event \rightarrow track \rightarrow step \quad .$$

In figure 4.2 the hierarchy is given as an example of a run with three events and six tracks (track number **(5)** turns into track number **(6)**). The dotted box is a run including the three events **(a)**, **(b)** and **(c)**. The number of tracks is the sum of all tracks in each event. A track possesses an initial state when it is generated and a final state when it is terminated. Between these states are the intermediate states that are calculated via different equations and can be part of the output if enabled. Calculating the final step of a track leads to the initial step of the next track until all tracks of an event are finished. If all events in a run are simulated, the run itself finishes. A simulation is finished if all runs are finished.

4.1.2 Particle generation

There are many possibilities to generate particles in KASSIOPEIA. First of all, the particle itself has to be characterized (e.g. mass, charge, spin) in the source code. A particle identification number (*pid*) links predefined particles with a number that serves as a shortcut, i.e. the pid of electrons is 11.

After setting the kind of particle, further information on that particle have to be declared. Those are energy, position, direction and starting time. Values for these parameters can be set in various ways. It is possible to set a constant value, values from a formula or a

completely random value (e.g. from a histogram input). With these start parameters the particles get their initial state.

4.1.3 Propagation of particles

Starting the tracking simulation, KASSIOPEIA begins with the calculation of different predefined values with each step the particle takes. Position, energy, momentum, magnetic field, electric potential are just a few of all parameters available. To calculate the position and additional values, equations of motion have to be solved. These equations have the form of first order ordinary differential equations. Therefore, integrating the equation becomes inevitable. KASSIOPEIA makes use of the numerical method called Runge-Kutta integrator of the 8th order [41]. Since the simulation has to reflect the reality as good as possible, more and more effects have to be considered, like relativistic motion or synchrotron radiation for charged particles.
In KASSIOPEIA, tasks regarding particle tracking are divided into:

- **trajectory:** different trajectory types can be set up like the *exact trajectory* or the *adiabatic trajectory* (see chapter 3).
- **control:** defines the step size that a particle has to travel before calculating all needed values
- **termiator:** sets up death conditions for particles like geometrical boundaries in from of volumes or surfaces and conditions like maximum/minimum position, radius, energy and more.
- **navigator:** the navigator monitors the state of the particle like making sure it propagates only in the defined geometries. It also checks if the particle meets a termination condition.
- **writers:** important particle states like initial state and final state or values that are calculated step by step are written in a ROOT file. Visualization of tracks can also be displayed via ROOT.

Calculating a step of a track that meets a termination condition terminates the particle. The state of that step becomes the final state of the particle and the track is completed. It is important to avoid infinite calculation of particles by setting correct termination conditions, otherwise valuable computer time is wasted.

4.1.4 Calculating electric and magnetic fields

As electric and magnetic fields determine position and direction of tracked particles, their fast and precise calculation has to be guaranteed to save computing time and memory.

4.1.4.1 Magnetic field calculation

Magnetic fields are generated through moving charges. A physical description of the magnetic field in a position $\vec{r}$ is given by the Biot-Savart's law

$$\mathrm{d}\vec{B} = \frac{\mu_0}{4\pi} \cdot I \frac{\vec{r} - \vec{r'}}{|\vec{r} - \vec{r'}|^3} \times \mathrm{d}\vec{s} \tag{4.1}$$

with an electric current I that flows through the infinitesimal line segment $\mathrm{d}\vec{s}$ located on position $\vec{r'}$ and the magnetic permeability μ_0. More complex geometries can be approached by splitting the current into discrete line current segments I_i. Calculating the magnetic

field for each segment, the total magnetic field can be calculated by summing all magnetic field segments $\vec{B}_i$

$$\vec{B}(\vec{r}) = \sum_{i=1}^{N} \vec{B}_i(\vec{r}) \quad . \tag{4.2}$$

Smaller and more precise line current segments result in a more precise total magnetic field. However, smaller segments require more computing time and more computer memory.

Using elliptic integrals

Since KATRIN uses axial symmetric magnetic field, elliptic integrals and zonal harmonic field expansion can be used for this case. For an infinitesimal thin solenoid the axial and magnetic field components B_r and B_z can be derived by

$$B_r = \hat{B}_z(Z_{max}) - \hat{B}_r(Z_{min}) \tag{4.3}$$

and

$$B_z = \hat{B}_z(Z_{max}) - \hat{B}_z(Z_{min}) \quad . \tag{4.4}$$

$\hat{B}_r$ and $\hat{B}_r$ are calculated by elliptic integrals to

$$\hat{B}_r(Z) = -\frac{\mu_0 \lambda}{\pi} \cdot \frac{(z-Z)R}{(r+R)S}[K(k) + \frac{R-r}{2R}(\Pi(n,k) - K(k))] \tag{4.5}$$

and

$$\hat{B}_z(Z) = -\frac{\mu_0 \lambda}{\pi} \frac{R}{S}[2\frac{E(k) - K(k)}{k^2} + K(k)] \quad . \tag{4.6}$$

$K(k)$ (**I**), $E(k)$ (**II**) and $\Pi(n,k)$ (**III**) are the respective elliptic integrals

$$K(k) = \int_0^{\pi/2} \frac{\mathrm{d}\theta}{1 - k^2 \sin^2\theta} \quad , \tag{4.7}$$

$$E(k) = \int_0^{\pi/2} \sqrt{1 - k^2 \sin^2\theta}\mathrm{d}\theta \quad , \tag{4.8}$$

$$\Pi(n,k) = \int_0^{\pi/2} \frac{\mathrm{d}\theta}{(1 - n^2 \sin^2\theta)\sqrt{1 - k^2 \sin^2\theta}} \quad . \tag{4.9}$$

The parameters for the equations above are

- $S = \sqrt{(r+R)^2 + (z-Z)^2}$,
- $k^2 = \frac{4Rr}{S^2}$,
- $n^2 = \frac{4Rr}{(r+R)^2}$,
- and λ as the linear current density.

With the help of the elliptic integral method, it is possible to calculate the magnetic field anywhere in the space without splitting the field generating coil into many small components. The counterpart, however, is the increase of the computing time needed to calculate these elliptic integrals [40].

Zonal harmonic expansion

The zonal harmonic expansion ([42]) offers a faster method to calculate the magnetic field. In this method, the magnetic field for a point $p(r, z)$ is expressed by Legendre polynomial expansion terms and their derivative at a source point z_0 on the symmetry axis [40]. For a point p that is located within a convergence radius ρ_{cen} of its source point z_0 and the distance ρ between p and z_0 the magnetic field can be calculated as

$$B_r = -\sin\theta \cdot \sum_{n=1}^{\infty} \frac{B_n^{cen}}{n+1} \cdot \left(\frac{\rho}{\rho_{cen}}\right)^n \cdot P_n'(\cos\theta) \quad , \tag{4.10}$$

$$B_z = \sum_{n=0}^{\infty} B_n^{cen} \cdot \left(\frac{\rho}{\rho_{cen}}\right)^n \cdot P_n(\cos\theta) \quad , \tag{4.11}$$

with $P_n(\cos\theta)$ as the n grade Legendre polynomial and B_n^{cen} the corresponding source point coefficients. For small ratios of (ρ/ρ_{cen}) the central convergence expansion converges faster and shows the advantage of large numbers of source points. But each coefficient requires a number of coefficients that need to be calculated beforehand. To calculate magnetic fields outside of the convergence radius, the remote convergence radius ρ_{rem} has to be considered. This results in

$$B_r = -\sin\theta \cdot \sum_{n=2}^{\infty} \frac{B_n^{rem}}{n+1} \cdot \left(\frac{\rho_{rem}}{\rho}\right)^{n+1} \cdot P_n'(\cos\theta) \quad , \tag{4.12}$$

$$B_z = \sum_{n=2}^{\infty} B_n^{rem} \cdot \left(\frac{\rho_{rem}}{\rho}\right)^{n+1} \cdot P_n(\cos\theta) \quad , \tag{4.13}$$

with B_n^{rem} as the remote coefficients. Here again, the central expansion will convergence faster for small (ρ_{rem}/ρ) ratios. Central and remote coefficients depend on the geometry as well as on the entered currents and will be stored for faster initialization for future simulations with same conditions.

Despite being faster than the elliptic integrals method, the zonal harmonic expansion can not calculate the magnetic field at any point (e.g. near coils). To be able to have a global magnetic field calculation, both methods will be used. Tracking particles inside the beam tubes makes up the biggest part of the simulation run by KASSIOPEIA permitting the use of the zonal harmonic expansion [40],[42].

4.1.4.2 Electric field calculation

An electric field is defined by the charge density distribution and the surface that encloses them. The charge density distribution depends on the voltage that is applied on the electrodes and the geometry of the electrodes itself. The general expression for the electric field is

$$\oiint_{\partial V} \vec{D} \cdot \mathrm{d}\vec{A} = \iiint_V \rho \mathrm{d}V = Q(V) \tag{4.14}$$

with $\vec{D}$ as the electric displacement field (that, in vacuum, is equal to $\vec{E}$, the electric field in vacuum), ρ the charge density and $Q(V)$ the total charge in a space. There are different solving approaches that depend on the type of the geometry. Axial symmetric geometries

for example can be solved by using elliptic integrals and zonal harmonics expansion similar to the magnetic field. One way of saving precious computing time is to split geometries in simpler structure components to ease up the calculation. The Boundary Element Method (BEM) does the same, splitting geometries in smaller parts that are assumed to have a homogeneous charge density. The approximation of a geometry S that is divided into N elements

$$\sum_{j=1}^{N} S_j \tag{4.15}$$

is more accurate when it is made up by a large number of elements ($N \to \infty$) so as the assumption of a homogeneous charge density distribution is more and more justified. Yet, again computing time and memory consumption have to be considered when approaching large numbers sub-elements of geometries.
The first step calculates each charge density σ_j of those sub-elements S_j by

$$U_i = \sum_{j=1}^{N} C_{ij}\sigma_j \tag{4.16}$$

with the Coulomb-matrix-elements $C_{ij} = C_J(\vec{r_i})$ and

$$C_j(\vec{r_i}) = \frac{1}{4\pi\epsilon_0}\int_{S_j} \frac{1}{|\vec{r_i} - \vec{r_S}|}\mathrm{d}^2\vec{r_S} \quad . \tag{4.17}$$

The calculation of the electric potential at a point $\Phi(\vec{r})$ can be performed according to equation 4.16 by integrating over all charge densities σ_j, which is

$$\Phi(\vec{r}) = \frac{1}{4\pi\epsilon_0}\int_{S_j} \frac{\sigma(\vec{r_S})}{|\vec{r_i} - \vec{r_S}|}\mathrm{d}^2\vec{r_S} \quad . \tag{4.18}$$

As stated above, larger numbers of sub-elements require high computing time and memory for the calculation. After calculating once, KASSIOPEIA caches the results for future simulations which have equal conditions [40].

4.2 Extending the source code

In the context of this work, two position generators were added to the KASSIOPEIA source code as they were needed for preparatory simulations. The *homogeneous flux tube generator* places particles homogeneously in a flux volume and the *multiplicity generator* imitates a scattering event of β^--electrons with residual gas where secondary electrons are generated. Magnetic field lines penetrating a surface define the magnetic flux over the surface (see equation 3.5). The radius for an axial-symmetric magnetic field increases with decreasing magnetic field strength and vice versa. Along the symmetry axis of the magnetic field the surface of the radii results in a surface which encloses a volume, called the *flux tube*. Generating particle inside the flux tube is of great interest because it is the relevant volume in which signal electrons propagate.

4.2.1 Homogeneous flux tube generator

Particles that are within the flux tube of $\Phi = 191\,\mathtt{Tcm}^2$ are detected at the detector. Particles outside of this volume are meant to hit on the components of the experiment and, thus, are not visible (if they do not scatter or change their movement differently). As only particles inside the flux volume are visible, computing time can be saved by distributing them in the flux tube and ignoring the space outside the flux tube.

The homogeneous flux tube generator uses the *flux tube generator* from S. Groh as a template and adds the function of distributing particles homogeneously in the flux tube. In order to achieve this, the generator calculates the maximal radius r_{max} of the flux tube along an axis (here $z - axis$) with the endpoints z_{min} and z_{max} that are predefined. Particles are then randomly generated in a cylinder with the volume

$$V = \pi(1.1 \cdot r_{max})^2 \cdot (z_{max} - z_{min}) \quad . \tag{4.19}$$

The radius of the ground surface has a tolerance factor of +10%.

Three parameters are calculated to set a particle in a volume. First, the position on the z-axis. Second, the radius (distance to the z-axis) and last, an angle (analog to polar coordinates). While the position on the z-axis and the angle are randomly chosen between two input parameters, the value for the radius is calculated between $r_{\min} = 0$ and $r_{\max} = r$ where r is the point at which the predefined flux is reached. The generator has the following input parameters

- *name* sets the name of the position generator,
- $flux$ defines the magnetic flux value to calculate the maximal allowed radius along the z-axis,
- *radius* sets up a maximal radius (can be left empty),
- $z_{\min}$ defines the minimal z-axis value,
- $z_{\max}$ defines the maximal z-axis value,
- $\phi_{\min}$ defines the minimal polar angle,
- $\phi_{\max}$ defines the maximal polar angle,
- *n_integrator_steps* sets up the precision of the numeric integration,
- *magnetic_field_name* defines the magnetic field of the simulation.

After a particle is set randomly in the cylinder a rejection sampling is processed. First of all, it is checked whether the particle is located in the flux tube. If it is within the flux tube, the particle is generated. If the particle is outside of the volume, the particle is rejected and another particle is randomly set in the cylinder, again with following location check. This leads to a bias towards larger flux tube radii and, thus, to a homogeneous distribution of particles in the flux tube. Figure 4.3 shows the homogeneity in a small section $\Delta z = 10\,\mathrm{mm}$.

4.2.2 Multiplicity generator

After a scattering event of high energy primary electrons coming from β-decay, secondary electrons are created. These second electrons are located on the same flux tube surface as the scattered primary particle (see chapter 5 for further information). Imitating this

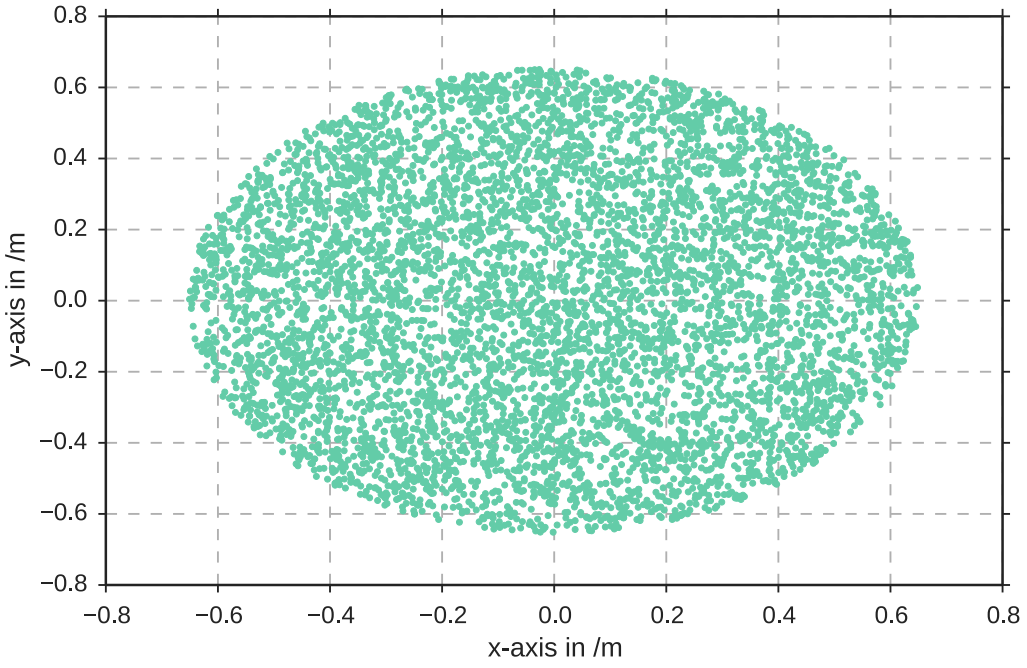

Figure 4.3: Display of homogeneity in the flux tube. A small section of $\Delta z = 10\,\text{mm}$ (from $-14.24\,\text{m}$ to $-14.25\,\text{m}$) is shown here with the position of the particles. In this picture the homogeneity is better visible.

event means to generate particles that follow magnetic field lines of the same magnetic flux. This can be done by setting one particle randomly in a flux tube with position z_0 and radius r_0. Calculating the magnetic flux Φ_0 via equation 3.5 allows to distribute a number of n particles p_i. It is then

$$p_i = p_i(r_i, z_i, \Phi_0) \tag{4.20}$$

with

$$\Phi_1 = \Phi_2 = \Phi_3 = \cdots = \Phi_n \quad . \tag{4.21}$$

With the conservation of the magnetic flux and axial-symmetric magnetic field each field line with equal magnetic flux hits on the detector in the same distance r from the center. Therefore, the circumference of a circle on the detector, with the center of the detector as the origin of the circle, defines the points with equal magnetic flux. Thus, all p_n particles that are generated should have the same radius at a given point on the symmetry-axis. In figure 4.4 these rings can be seen when they are generated (left) and at the end when they are terminated (right).

These generators were created to obtain better parameters for electrode potentials and solenoid currents through preparatory simulations, i.e. increasing the amount of electrons that hit on the detector. The configuration with the best signal is then adopted later for larger simulations. Furthermore, the generators allow to check whether experimental ideas based on these generators are worth working on.

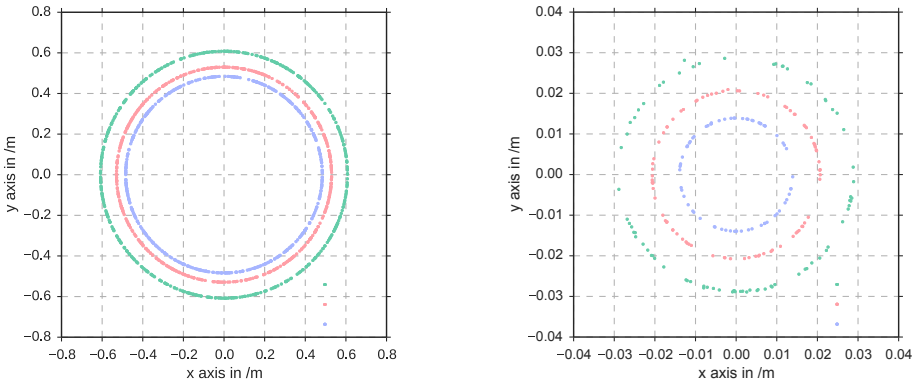

Figure 4.4: Particles generated with equal magnetic flux values. Left: Three events were started with 1000 particles each, resulting in a circular pattern at position $z = -14.25\,\mathrm{m}$. **Right:** Again three events were started with 100 particles in each event at the same magnetic flux. The particles that could reach the detector were terminated at the pinch magnet (to safe computer time). All three ring structures are clearly visible.

5. Stored-particle induced background

In every particle physics experiment it is necessary to reduce disruptive factors as much as possible. To do that it is of utmost importance to analyze the characteristics of these factors and to determine their origin. In this chapter a possible background source in term of tritium entering the PS is described, how it can be identified and how it is potentially possible to take advantage of this background source to learn about the effectiveness of tritium retention in the CPS.
The main focus of this work is the feasibility study whether tritium flow from he CPS to the PS is detectable via secondary electrons generated by tritium decay in the PS and if it is possible to make a statement about the functionality of the CPS.

5.1 Tritium migration into the CPS

The vacuum pumps of the DPS and the CPS have the task to reduce the tritium flow to the PS by the factor 10^{14}. It is still possible for a tiny amount of tritium to diffuse to the PS. As tritium occurs mainly as molecular compound of hydrogen and tritium (**HT**), the following calculation for the gas flow rate and the decay rate will be done for the case of **HT** molecules. Assuming a gas flow from the CPS to the PS

$$Q_{\mathrm{CPS}\to\mathrm{PS}} = 10^{-14}\,\mathrm{mbar\ l/s} = 10^{-15}\,\mathrm{Pa\ m^3/s} \tag{5.1}$$

leads via the ideal gas law to the following molecule flow rate

$$N_{\mathrm{CPS}\to\mathrm{PS}} = \frac{Q_{\mathrm{CPS}\to\mathrm{PS}}}{k_B T} = \frac{10^{-15}}{1.38\cdot 10^{-23}\cdot 293}\,\frac{1}{\mathrm{s}} = 2.5\cdot 10^{5}\,\mathrm{s}^{-1} \quad , \tag{5.2}$$

with k_B as the Boltzmann constant and T the temperature [35, 43]. From simulation a pumping speed $S_{\mathrm{PS}} = 40000\,\mathrm{l/s}$ of the getter pumps in the PS can be derived for HT gas. The molecular mass M dependence of the pumping speed is $S \sim 1/\sqrt{M}$. The partial pressure for HT in the PS is then given by

$$p_{\mathrm{PS}} = \frac{Q_{\mathrm{CPS}\to\mathrm{PS}}}{S_{\mathrm{PS}}} = 2.5\cdot 10^{-17}\,\mathrm{Pa} \quad . \tag{5.3}$$

Again with the ideal gas law the number density of **HT** molecules can be calculated by using the partial pressure in equation 5.3. The value for the number density n_{PS} is then

$$n_{\mathrm{PS}} = \frac{p_{\mathrm{PS}}}{k_B T} = 6200\,\mathrm{m}^{-3} \quad . \tag{5.4}$$

To get the total number of HT molecules, equation 5.4 has to be multiplied by the volume that is filled by the molecules. As only particles inside the flux tube are visible at the

detector, only the volume of the flux tube is considered. The flux tube in the PS is created by two coils at both ends of the PS named PS1 (towards CPS, *upstream*) and PS2 (towards MS, *downstream*). With a magnetic field of $B_{\mathrm{PS1/PS2}} = 4.5\,\mathrm{T}$ and a magnetic flux of $\Phi = 191\,\mathrm{Tcm}^2$, a volume V_{PS} of

$$V_{\mathrm{PS}} = 2.2\,\mathrm{m}^3 \tag{5.5}$$

is filled up. Together with the number density the total number of HT molecules in the PS is

$$N_{\mathrm{PS}} = n_{\mathrm{PS}} \cdot V_{\mathrm{PS}} = 13600 \quad . \tag{5.6}$$

So even with a reduction factor of 10^{14} from the transport section, a significant number of tritium molecules is present in inside the PS. With the β-decay rate of HT molecules of

$$\lambda_{\mathrm{HT}} = 1.79 \cdot 10^{-9}\,\mathrm{s}^{-1} \tag{5.7}$$

the total β-decay rate of all **HT** molecules within the PS flux tube can be calculated to

$$D_{\mathrm{PS}} = 2.4 \cdot 10^{-5}\,\mathrm{s}^{-1} \quad . \tag{5.8}$$

With this it may be estimated that every $24 \cdot 10^6\,\mathrm{s}$ a β-decay occurs in the PS. This estimate has to be experimentally be confirmed.

5.2 Background characteristics

As mentioned in chapter 3, particles generated in a low-magnetic field can be trapped if the magnetic field increases on both sides by being reflected by the magnetic mirror effect on both ends. In this case tritium β-decay in the PS generates high energy primary electrons. These electrons perform three kinds of motion. First the cyclotron motion by following a magnetic field line, second an axial motion due to the reflection of the magnetic mirror effect and third a magnetron drift resulting from the gradient of the magnetic field $\vec{\nabla}B$. Figure 5.1 shows all three motions of a primary electron coming from tritium β-decay with a kinetic energy of $E_{\mathrm{kin}} = 1\,\mathrm{keV}$.

The trapped primary electrons eventually scatter with residual gas and generate secondary electron that possess lower energies. The lower energy electrons are able to leave the trap and reach the detector causing a background signal.

Considering adiabatic motion and the conservation of the magnetic flux, secondary particles follow the magnetic field line where they were generated until they hit on the detector. The magnetron drift of the primary electron results in a ring shaped event pattern on the detector. As scattering events are rather rare because of the low pressure in the spectrometer tanks, the detector does not only register hits from the secondary electrons, but also signals from other (uncorrelated) background making it impossible to assign a single background event to one decay. To speed up the cool-down process of the primary particle, many scattering events need to happen in a short time. This can be achieved by elevating the pressure in the spectrometer artificially to $10^{-8}\,\mathrm{mbar}$ [45].

Figure 5.2 shows the average storage time of electrons at different pressures. The higher the energy of the electron, the larger the storage time in the spectrometer and the higher the pressure of the spectrometer tank is, the shorter the storage time gets.

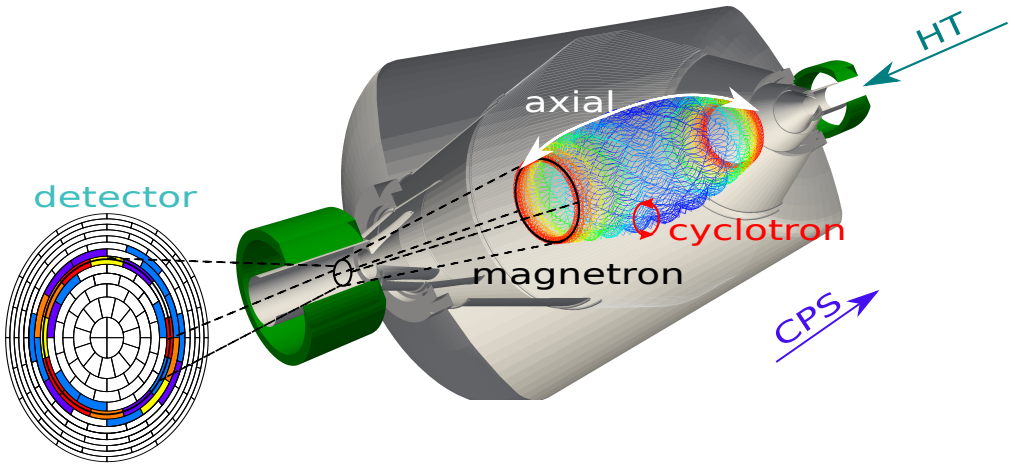

Figure 5.1: Stored β-electron in the PS. Simulation of a β-electron with a kinetic energy of $E_{kin} = 1\,\text{keV}$. There are three different motions that are performed by the particle. The cyclotron motion is executed when a charged particles enters a magnetic field and follows a field line. The axial movement of the particle comes from the magnetic mirror effect. With each reflection by the magnetic mirror, the particle shifts its position resulting in the magnetron drift. The divergence of the magnetic field $\vec{\nabla}B$ causes this drift. If a scattering event happens, secondary electrons are generated. These electrons follow the same field lines as the primary particle and hit on the detector in a circular pattern. This is possible since the magnetic flux is conserved (see chapter 3). It is important to note that the ring shape is not visible at normal operating pressure due to the long cool-down times of the primary electron which makes it impossible to differentiate single secondaries from other uncorrelated backgrounds. Artificially elevating the pressure in the spectrometer, however, decreases the cool down time and allows to identify single rings/decays. Figure adapted from [34, 44].

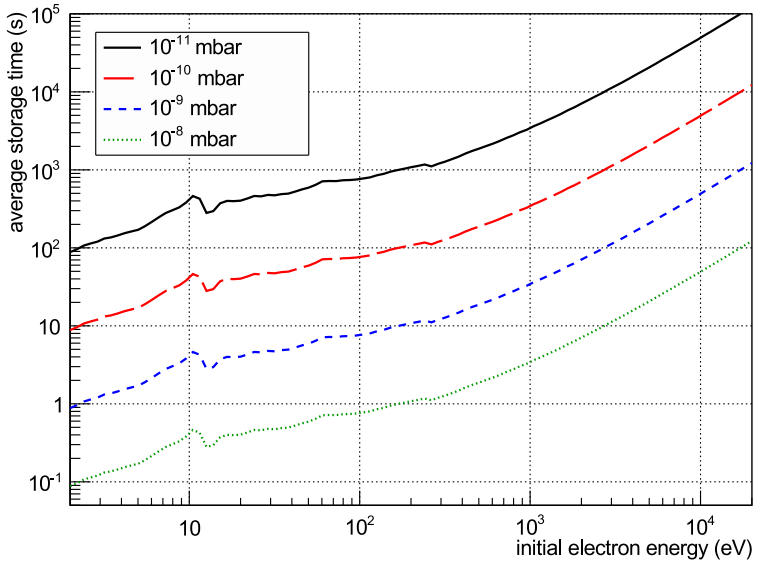

Figure 5.2: Storage time of electrons in the MS at different pressures. With increasing pressure, scattering events happen more often. The probability of scattering events between primary electrons and residual gas is higher with increasing pressure, resulting in shorter average storage times of primary electrons. Figure taken from [45].

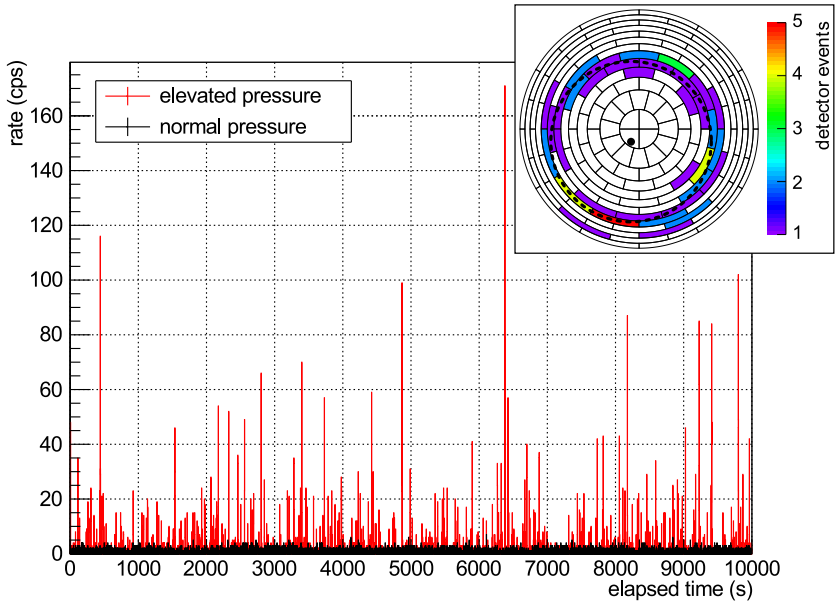

Figure 5.3: Detector hit rate at normal pressure and at elevated pressure. The figure shows the rate of secondary electrons that were generated by radon decay at the detector over time. The red line represents the elevated pressure, the black line represents normal pressure. With higher pressure more electrons reach the detector in short time frames, as the scattering rate of primary particles increases. These large numbers coming in *spikes* are referred as *clusters* and the secondary electrons making up a cluster are called *cluster events*. The hits on the detector resemble a ring and the color code shows the intensity on each detector pixel. Figure taken from [45].

In figure 5.3 the rate of the detector hits is displayed over time at normal pressure and at elevated pressure. Higher pressure resulting in increasing scattering rates leads to a high number of secondary electrons in shorter time frames. These secondary electrons hit on the detector as *cluster events*, building up a *cluster*. Particles from a cluster are distributed in a circular pattern over the detector, confirming the assumed characteristics of this background. In this case radon α-decay is the background source.

As this background source is already well known by radon experiments, for an initial approach it can be used for tritium, too. To sum it up, stored-particles induced background can be detected by decreasing the storage time in the spectrometer.

5.3 Detecting β-decays in the PS

To detect a single tritium decay in the PS means to identify cluster events at the detector and assign them to a cluster. The upcoming problem is to filter the other (uncorrelated) background sources. Furthermore, the average number of secondary electrons generated by a tritium decay has to be known as well as the fraction of the secondary electrons that is able to reach the detector. The analysis algorithm and interpretation of simulation data is part of chapter 6.

5.4 Checking the functionality of the CPS

A good way to make use of tritium decaying in the PS is to check the functionality of the CPS. With the CPS freshly regenerated, the number of tritium decays in the PS gives an idea of the functionality of the CPS. In this context, it is important to block every ion/electron coming from the tritium source to have only the background signal from the

Table 5.1: Preparatory simulation - symmetric potential configuration with 100 A LFCS setting. In the first preparatory simulation a symmetric electric field configuration was used. This means that both full-metal cone electrodes of the PS are set to the same potential.

electrode	potential in kV
hull electrode	-18.0
inner electrode (wire)	-18.4
upstream cone electrode	-18.7
downstream cone electrode	-18.7

PS. This can be done by setting the potential of the upstream side full-metal cone electrode of the PS higher than the decay energy of tritium, i.e. $qU_{\mathrm{PS}} > 18.6\,\mathrm{keV}$. First the valve between the CPS and PS is closed and only the background signal of the PS is measured. After that the valve is opened again and the background of the PS is measured together with a potential background due to tritium decay in the PS. With these two measurements it is in principle possible to estimate the decay rate of tritium in the PS and, thus, estimate the functionality of the CPS.

5.5 Preparatory simulations

Simulation close to the reality take long computing times. To have approximately ideal parameters, it is necessary to simulate parts of the physical process separately. Faster and simpler simulation help with setting up the boundary conditions of a more time consuming simulation, promising faster success. In case of tritium β-decay in the PS, it is of utmost importance to guide all generated secondary electrons to the detector. Hence a close examination of the electromagnetic configuration is needed to achieve the best guidance condition for secondary electrons. Another important aspect is to check for the arrival probability of the electrons in dependence of their initial radius in the PS.

5.5.1 Simulation parameters

Allowing only tritium to diffuse to the PS and blocking all signal electrons coming from the WGTS requires a blocking potential higher that the maximal kinetic energy a tritium β-electron can have. Table 5.1 shows the potential configuration inside the PS. The full-metal cone electrodes have a potential of $-18.7\,\mathrm{kV}$ and, thus, fulfill the task of blocking signal electrons that can have a maximum kinetic energy of $E_0 = -18.6\,\mathrm{keV}$. The currents of the 14 air coils of the MS are set to 100 A each, except the last air coil, that can not run on this high currents. The reason for the high LFCS currents is, that a higher magnetic field guides the signal electrons more effective to the detector.

In the first preparatory simulation 10^6 electrons were generated homogeneously distributed in the flux tube of the PS using the *homogeneous flux tube generator* (see chapter 4). The particles are started with isotropic starting angles and an initial energy diced from a theoretical energy distribution calculated in [46] (see figure 5.4).

Relevant particle termination commands for all preparatory simulations are:

- *exit_upstream*: terminated by exiting the PS to the CPS,
- *trapped_ps*: particle changing its direction more than four times in the PS, thus, considered being trapped in the PS,
- *trapped_ms*: particle changing its direction more than four times in the MS, thus, considered being trapped in the MS,

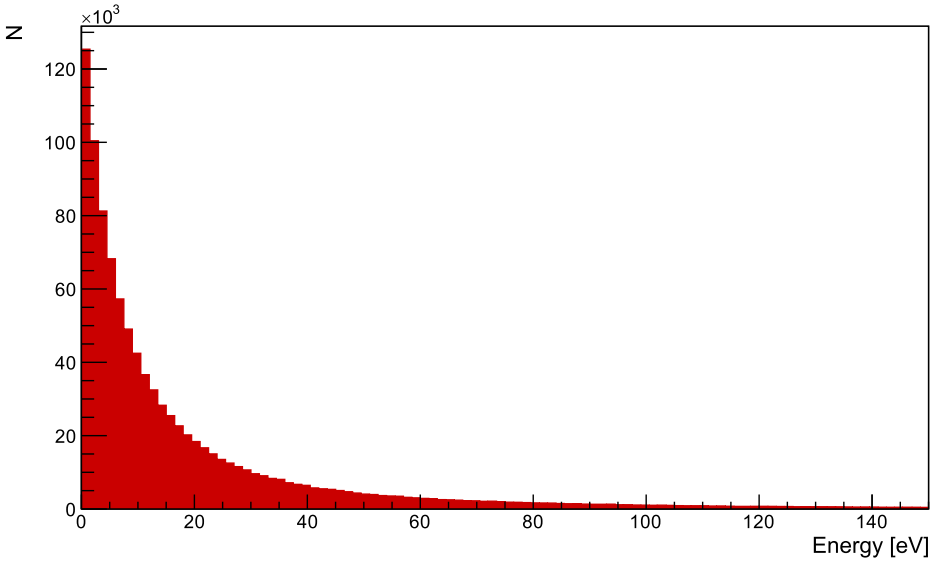

Figure 5.4: Theoretical energy spectrum of secondary electrons from tritium decays in the PS. Figure adapted from [46].

- *trapped_global*: particle changing its direction more than four times in the PS and MS, thus, considered being trapped between PS and MS,
- *detector_hit*: particle hits on the detector and is terminated.

In figure 5.5 the result of the first simulation shows that roughly 10% of the started electrons reached the detector. To increase the detector signal, i.e. increase the rate of secondary electrons reaching the detector, the electromagnetic configuration has to be optimized. Setting the current of the first thirteen air coils to 180 A reduces the amount of stored particles in the MS due to higher magnetic fields and, thus, a more adiabatic motion of the particles. A higher difference between B_{min} and B_{max} shifts the maximal angle of the electrons higher and allows more electrons to reach the detector (see trapped particles in chapter 3). With a symmetric potential configuration the electrons are able to leave the PS in both direction. The fraction of the secondary electrons leaving towards the PS and the fraction that leaves towards the MS (detector termination + trapped termination in the MS) is about equal. Indeed, the results of the second simulation (see figure 5.6) show a decrease of stored particles in the MS while the fraction of electrons reaching the detector does increase. Again about the same amount of electrons leave the PS in both directions. To further increase the signal, the electrons that leave towards the CPS have to be stopped and guided to the detector.

A possible way to do that can be done by setting an asymmetric potential configuration of the PS electrodes. This means that both full-metal cone electrodes of the PS are set to different potentials. While the upstream electrode is still operating in a blocking mode, the potential on the downstream electrode is reduced, making it more likely for electrons to leave the PS towards the MS.

The final electrode configuration for the PS is shown in table 5.2 while figure 5.7 shows the corresponding simulation results. With about 85% of all electrons reaching the detector a significant improvement compared to the first simulation could be achieved.

Please note that the 180 A LFCS setting used in the simulations exceeds the technical specifications of the MS air coil system cited in table 5.3 [47]. However, the simulation

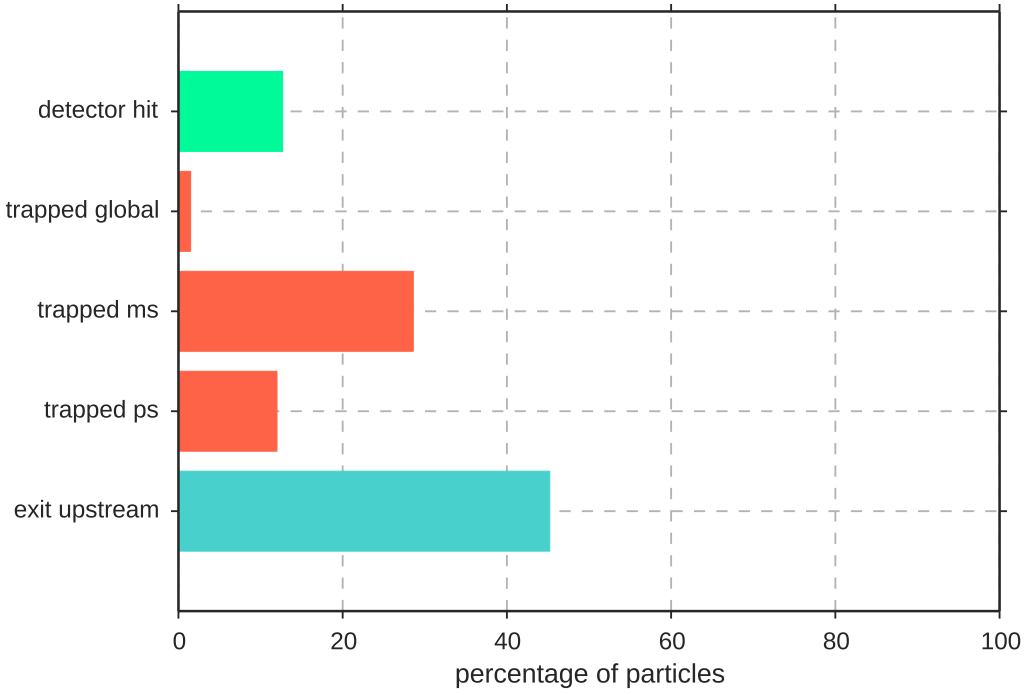

Figure 5.5: Termination of particles with 100 A LFCS and symmetric PS potential configuration. The majority of particles leaves the PS to the CPS, the rest is trapped and only a few particles reach the detector.

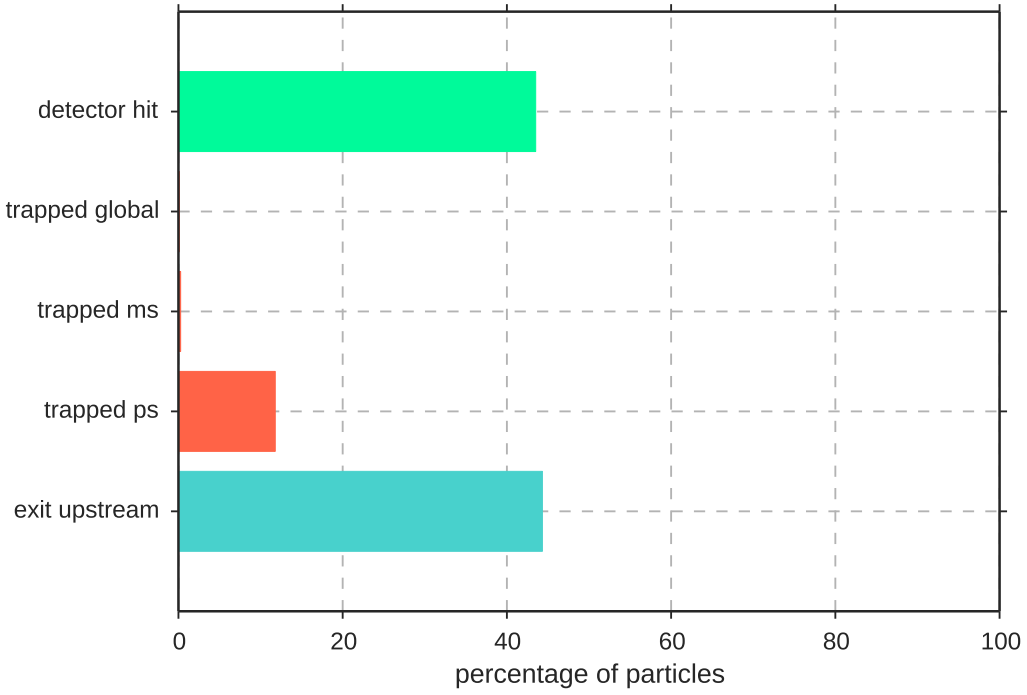

Figure 5.6: Termination of particles with 180 A LFCS setting and symmetric PS potential configuration. About the same amount of particle leave the PS to the CPS and to the detector. About ten percent are stored in the PS.

Table 5.2: Preparatory simulation - asymmetric potential configuration with 180 A LFCS. In the last preparatory simulation an asymmetric electric field configuration was used. This means that the two full-metal cone electrodes of the PS are set to different potentials. While the upstream cone is kept at a blocking potential the potential on the downstream cone is reduced. With this configuration electrons are less likely to leave the PS towards the CPS.

electrode	potential in kV
hull electrode	-18.0
inner electrode (wire)	-18.4
upstream cone electrode	-18.7
downstream cone electrode	-18.3

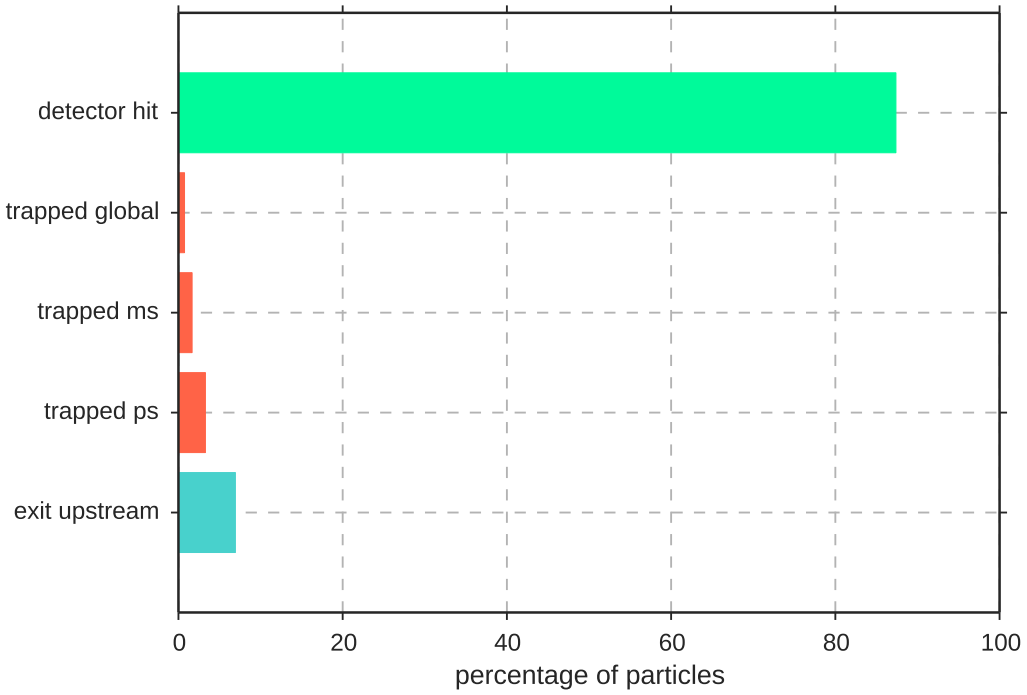

Figure 5.7: Termination of particles with 180 A LFCS setting and asymmetric PS potential configuration. Nearly 85% of the particles do reach the detector.

Table 5.3: Maximum current technical possible for LFCS coils of the MS.

air coil	max. current in A
1 & 2	100.0
3 - 11	175.0
12 & 13	100.0
14	70.0

results should not differ significantly if the maximum possible currents are used as the current in the air coils in the center of the MS are more important for the adiabatic motion of the particles. Test simulations with the air coil currents set to $I_{LFCS} = 160\,\mathrm{A}$ showed no significant differences.

5.5.2 Arrival probability of secondary electron clusters

Particles that start in PS are assigned to a ring on the detector. As there are not only one but several secondary electrons generated by a tritium decay in the PS, the detection probability of this secondary electron cluster has to be calculated. The following simulations possess the same electromagnetic configuration as in table 5.2.
There are two ways to determine the arrival probability of clusters on each detector ring, both of which were executed in the context of this thesis. The first method is rather straight forward and just focuses on simulations with increasing cluster sizes. However, it is time consuming and inefficient. Another way is to simulate the arrival probability for a single electron and then calculate the probabilities for higher cluster sizes. If $p_{\mathrm{ring,hit}}$ is the probability of an electron to reach a specific detector ring and $p_{\mathrm{ring,\ no\ hit}} = 1 - p_{ring,hit}$ is the probability of a particle to be terminated differently, then the probability of for higher cluster sizes is

$$p_{ring,n} = \sum_{i=k}^{n} \binom{n}{k} \cdot p^{i}_{\mathrm{ring,no\ hit}} \cdot p^{n-i}_{\mathrm{ring,hit}} \quad , \tag{5.9}$$

with n as the actual cluster size and k as the cluster size threshold that states the minimum number of electrons of a cluster event needed to count a tritium decay detection.

The arrival probability of single secondary electrons is shown in figure 5.8. A tendency of decreasing arrival rates with increasing ring number is observed.

With the probabilities for each ring given, it is now possible to calculate the arrival probability for any cluster size on any ring with the use of equation 5.9. As an crosscheck the probability for a cluster size of $n = 5$ was simulated with the first method and then compared to the result calculated with the second method. The left side of figure 5.9 shows the detection probability of secondary electron clusters calculated via equation 5.9 with $n = 5$ and $k = 2$. So two particles of in total five reaching the detector suffice to cause a detection. On the right side of figure 5.9 the arrival probability for the same cluster size as simulated according to method 1 is shown.

The values from the simulation are slightly smaller than the values calculated analytically. The tendency to higher rings however, is the same for both methods. Looking at higher cluster sizes, the detection rate increases as it is more likely to detect only two particles of a cluster with an larger number of particles. Figure 5.10 shows the analytically calculated cases for cluster sizes $2 - 10$. Cluster sizes of six or higher overlap each other as all values of 5.8 converge in equation 5.9 to 1.

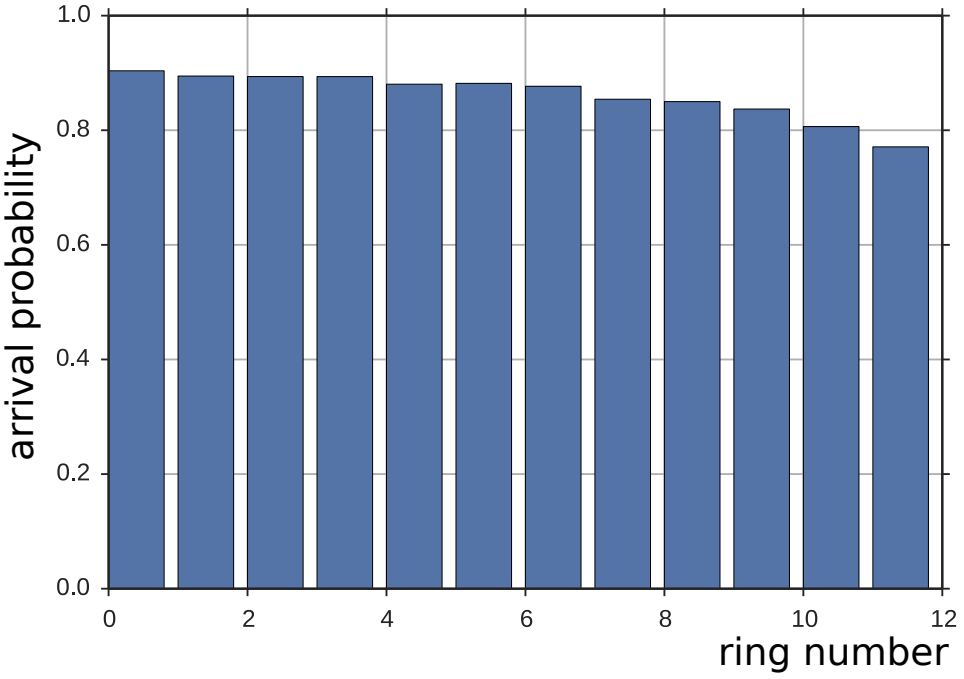

Figure 5.8: Arrival probability of single electron as a function of the detector ring. Electrons were started homogeneously in the PS with following electromagnetic configuration: asymmetric potential configuration in the PS and 180 A current on the MS air coils.

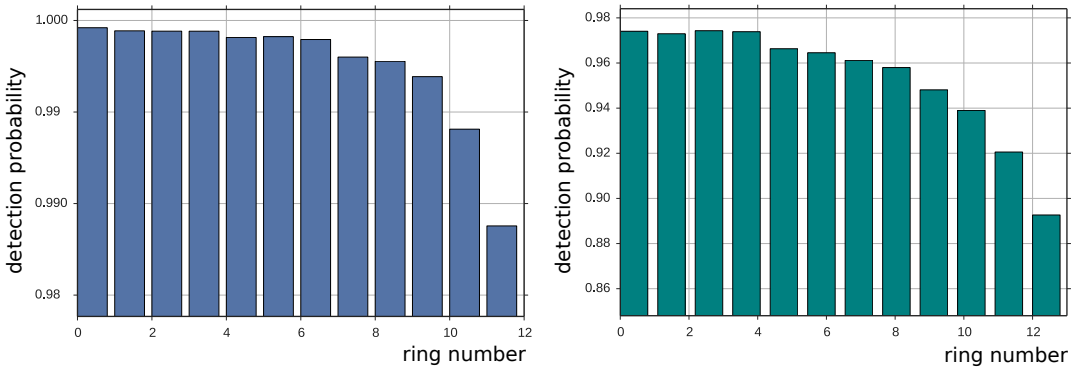

Figure 5.9: Detection probability of cluster sizes of 5 calculated and simulated. **Left:** Detection probability of a cluster with five electrons calculated via equation 5.9. **Right:** Detection probability of same cluster size simulated. The values of the simulation are slightly smaller but the tendency to higher ring numbers is the same for both.

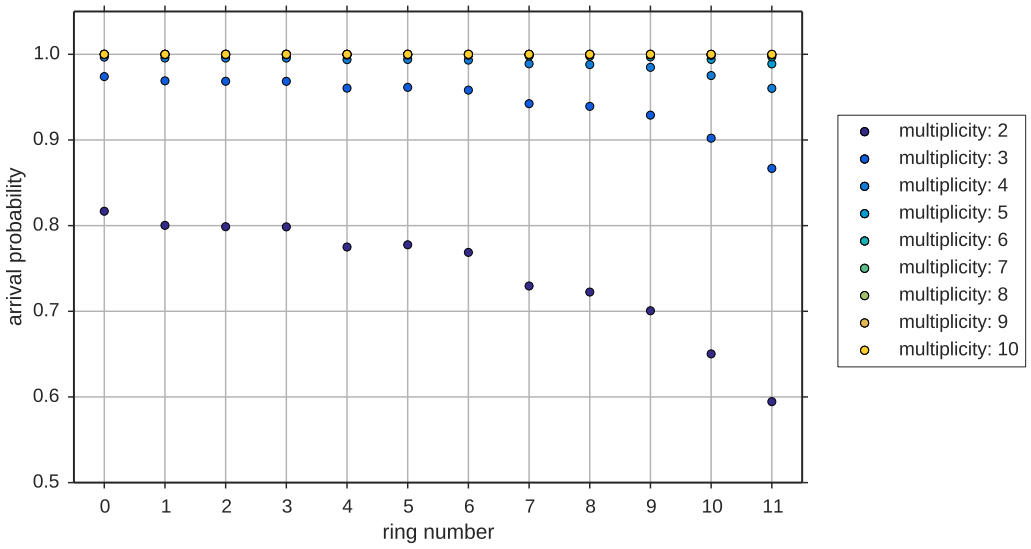

Figure 5.10: Detection probability of cluster sizes from 2 to 10. The detection probabilities converges to 1 for higher cluster sizes as it is more likely to detect two particles of a cluster with larger cluster sizes.

5.6 Outlook for storage simulation

For future storage simulation (see chapter 6) the air coils of the MS have to be set to the highest current possible in order to reduce the amount of stored particles in the MS. Furthermore, an asymmetric potential guides particles preferably towards the MS and blocks most particles towards the CPS. Concerning the detection probabilities, special configurations are not required in the storage simulation due to high detection probabilities for each ring and every larger cluster size.

6. Storage simulation

To detect tritium decays in the PS, the characteristic signal of stored particles in the spectrometer has to be detected in form of event clusters. For an actual simulation of stored-particles close to the reality the primary particles have to be tracked until they are fully cooled down (no trapped particle termination as in the preparatory simulations). During the storage process of the primaries, scattering events with residual gas can occur. Ionization of residual gas leads to secondary and tertiary electrons that have to be tracked, too. With the number of particles per tritium decay increasing, the simulation gets more and more time consuming as such a *storage simulation* with the KASSIOPEIA framework tracks all primary particles and secondary electrons until thermalization [40].
In this chapter the storage simulation results for electrons accompanying from tritium β-decay in the PS is discussed. The analysis of the simulation data plays a crucial role to understand future measurement data and makes up a major part of this chapter. A short summary about the feasibility of future experiments targeting a CPS functionality check via the detection of tritium β-decays in the PS concludes the chapter.

6.1 Simulation configuration

The PS potential configuration (see table 5.2) of the storage simulation is equal to the final preparatory simulations in chapter 5 for which a high signal to noise ratio from secondary electrons is expected. The air coils were set to 180 A, except air coil number 14 that was set to 70 A (note that the actual possible hardware configuration differs slightly from this set up, but the difference (table 5.3) is assumed to have a minor impact). All electrodes of the MS were set on zero potential. The simulation was done with the pressure in the PS set to 10^{-8} mbar as it is planned for future experimental set ups. The role of the residual gas was adopted by helium. A total of 10^4 primary particles were generated randomly in the PS volume (not only in the flux tube).

6.1.1 Generator and terminators

The event generator of the simulation imitates a radioactive β-decay and generates primary electrons randomly in the PS volume with a random energy by respecting the probability given by the β-spectrum between E_{min} and E_{decay}. In the case for tritium decay the minimal energy is $E_{\mathrm{min}} = 0\,\mathrm{keV}$ and the maximal energy is the decay energy of tritium $E_{\mathrm{decay}} = 18.6\,\mathrm{keV}$. Notable termination conditions are when

- particles cross the inner spectrometer surface,
- leave the PS towards the CPS,
- reach the detector,
- or fall below a total energy of $E_{\mathrm{tot}} = 15.6\,\mathrm{keV}$.

Secondary electrons generated in the PS are accelerated by the electrode potentials and are likely to have about the same magnitude of energy as the potentials. Thus, the origin of particles that have too much or too less energy can not be assumed in the PS. This leads to a region of interest (*roi*) and explains the terminator on the minimal total energy E_{tot} of a tracked particle.

6.1.2 Dynamic enhancement

A storage simulation tracks a stored particle from its generation to thermalization. An early termination of stored particles as used in the preparatory simulations would be contrary to the purpose of this simulation. A full tracking of stored electrons is needed and, therefore, leads to an enormous increase of computing time. Furthermore the energy dependent cross-section of electron helium scattering $\sigma_{e^-He} = \sigma_{e^-He}(E)$ is lower at higher electron energies. Primary electrons coming from tritium β-decay can possess high energies and, thus, are less likely to interact with helium. The β-electron loses its energy due to synchrotron radiation effects and then eventual scatters with residual gas. To accelerate the simulation process, an *enhancement factor* can be used.
With the enhancement factor enabled, each step calculation like i.e. scattering probability or energy loss due to synchrotron radiation loss is accelerated by that factor. First of all, two states of the particle are checked, namely, the last time stamp after an interaction and the current time stamp. The time difference of these values should not fall below a given minimal time. This verification exists to avoid unphysical propagation of particles, i.e a particle that would have terminated by crossing the spectrometer hull would fly back if exact after the last interaction another interaction would lead the particle back into the spectrometer. The option of a *dynamic enhancement* turns the enhancement factor into a variable value. The dynamic enhancement factor is inversely proportional to the cross-section and accelerates the simulation for smaller cross-sections more than for larger values, making the enhancement process dynamic. The time output of the tracks is corrected according to the factor that is multiplied by each step calculation. All in all, the dynamic enhancement compensates the energy dependent cross-section which is smaller for higher electron energies and increases for decreasing electron energies. For the storage simulation an enhancement factor of 1000 was used.

6.2 Analysis of simulation data

To be able to analyze the simulation results in the same way as real detector data the simulation data has to be converted into a format that can be used as an input for the standard data analysis code.

6.2.1 Imitating experimental data

The main task is if a clear signal of tritium decay in the PS is detectable using only the background afflicted pseudo data of the simulation. Reproducing the amount of tritium decays (in this simulation 10^4) would in general show the feasibility of this detection method. The activity $A(t)$ of tritium in the PS is given by an exponential law

$$A(t) = A_0 \cdot \exp^{-\lambda t} \tag{6.1}$$

with time t and λ as the exponential decay constant. Distributing the simulated events exponentially in a time frame with a given activity $D_{\mathrm{PS}} = 2.4 \cdot 10^{-5}\,\mathrm{s}^{-1}$ (see chapter 5) and adding that time to the time of each simulated track of an event, creates a time series of background-free pseudo data events. As background can not be neglected in an actual

experiment, the pseudo data has to be smeared by uncorrelated background events within the time frame of the tritium simulation. The rate for the uncorrelated background was set to $D_{\mathrm{BG}} = 50 \cdot 10^{-3}\,\mathrm{s}^{-1}$ [48]. In the end a time series of pseudo experimental-data is generated that can be analyzed by the analysis code as real experimental data.

6.2.2 Analysis code

As known from radon measurements, cluster events appear in relative short time intervals Δt [45]. So if a detector signal shows multiple hits in a specific time frame where each detector hit is within a certain time interval Δt, after the last count a cluster is detected. A single high energy β-electron coming from tritium decay generates a cluster of secondary electrons. Counting these cluster events and assigning them to a single cluster indicates an occurred tritium decay in the PS. Hence, it is possible to deduce the number of tritium decays in the PS by counting the clusters and cluster events. The main problem of this detection method is to find a time frame Δt that fits in the case of tritium. Another problem is to filter out accidental clusters generated by the uncorrelated background which lead to an increase of detected clusters and result in an overestimation of the tritium decays. In the case of simulation data the real number of tritium decays is known making it possible to improve the analysis code to achieve a higher detection efficiency. To sum it up the analysis code needs to detect clusters and distinguish them from accidental clusters that originate from uncorrelated background events.

6.2.2.1 Cluster detection

The first step in the cluster detection is a check of the interarrival time between events Δt. The analysis algorithm compares two consecutive time stamps t_i, t_{i+1} and checks if they arrive at the detector within a given time frame

$$t_{i+1} - t_i \leq \Delta t \quad . \tag{6.2}$$

If both cluster event times fulfill the requirement, the next time stamp t_{i+1} is compared with the last one t_i. This goes on until the two consecutive times do not appear within the given time frame $t_{i+1} - t_i \nleq \Delta t$. Subsequently, it is checked if the number of all consecutive time stamps that arrive in the given time window Δt exceed the cluster size threshold. If they do, the time stamps are recognized as cluster events and the cluster is added to the list of cluster sizes. If the conditions are not satisfied, the events are considered as background and the algorithm moves to a new set of arrival times. A schematic overview of the algorithm is given in figure 6.1.

6.2.2.2 Accidental detection

Apart from clusters made up by the correlated events from tritium decays they can also accidentally be made up by uncorrelated background events and being falsely registered by the cluster detection algorithm. Those fake clusters are called *accidental clusters*. To identify those accidentals another detection method has to be applied.

As the background is Poisson distributed the probability of finding single events in a time frame Δt should be equal to finding background events in a larger distance T within the same time window

$$T \leq t_{i+1} - t_1 < T + \Delta t \quad . \tag{6.3}$$

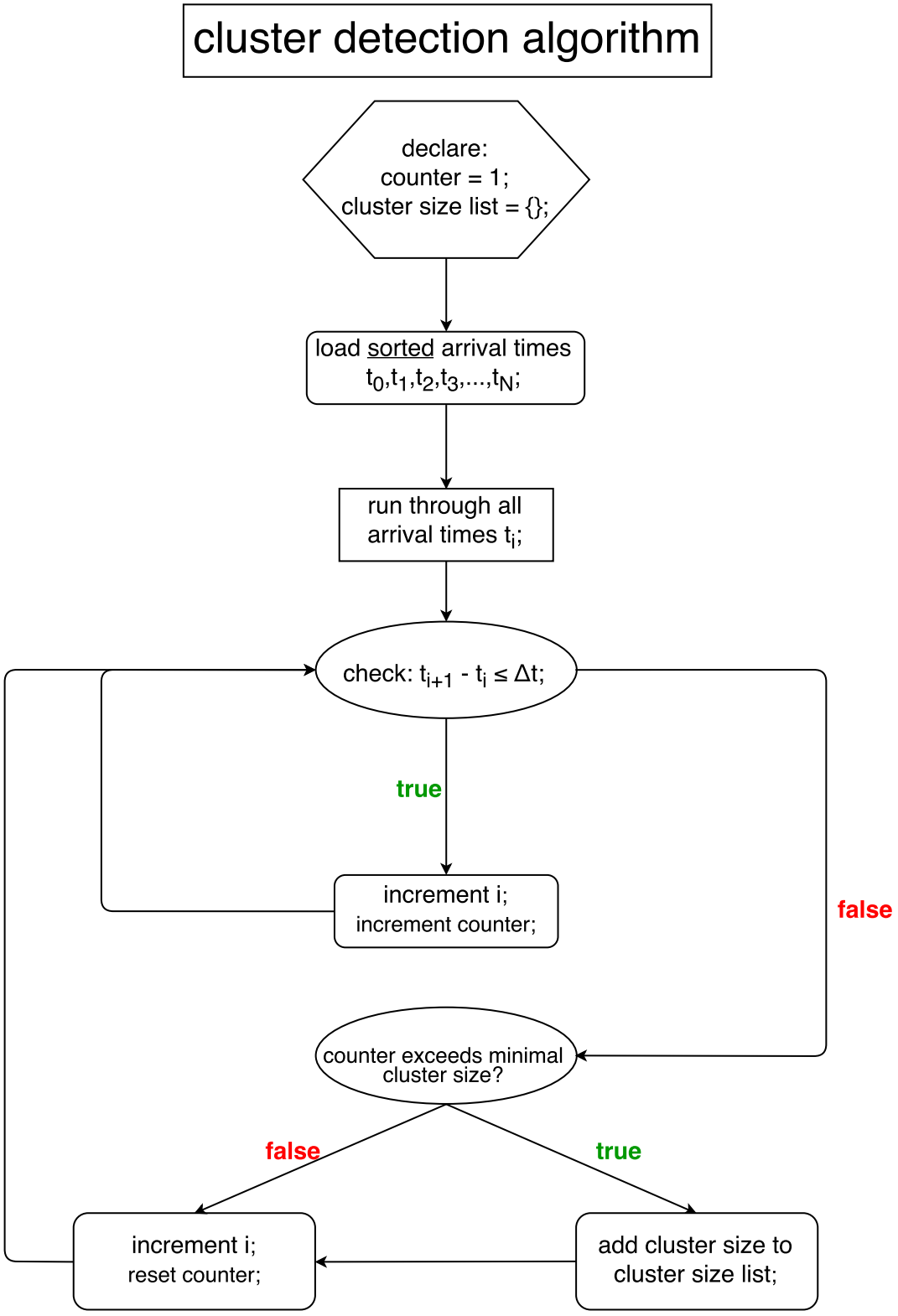

Figure 6.1: Schematic overview of the cluster detection algorithm.

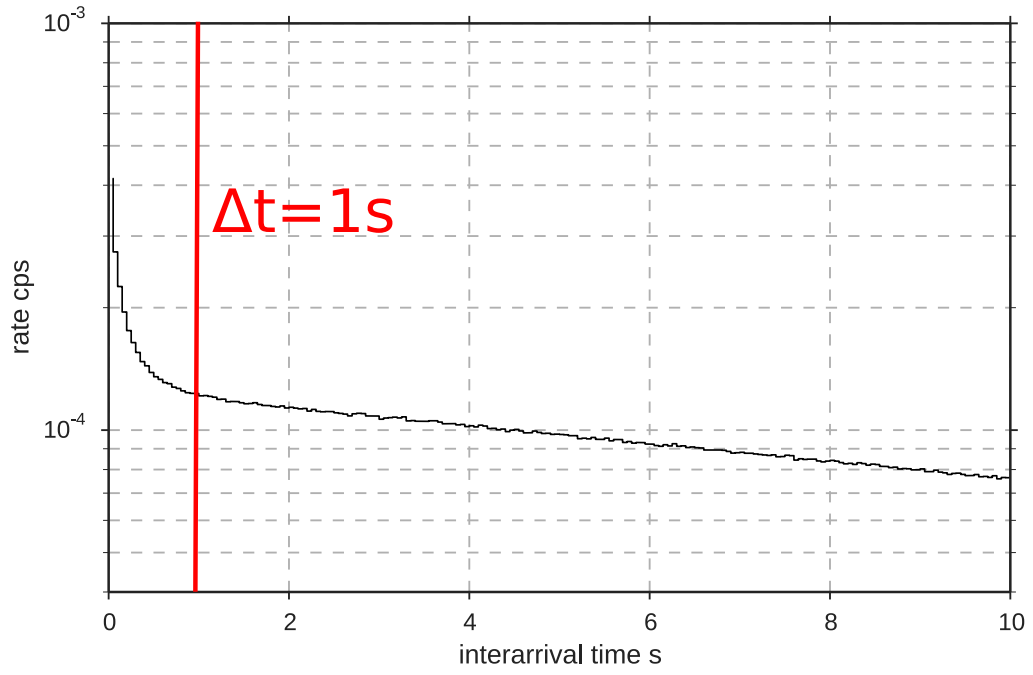

Figure 6.2: Interarrival times of cluster events coming from tritium β-decays. The majority of secondary electrons arrive in time frames shorter than $\Delta t_i = 1\,\mathrm{s}$. It can be assumed that a cluster forms in this time frame.

An additional condition for a fake signal detection is, that the checked cluster event is not the first cluster event of a cluster that was detected prior by the cluster detection algorithm. If both conditions are met, the compared arrival times are considered as background events and removed from the multiplicity histogram created by the cluster detection algorithm.

Note that these algorithms were used before for the same cause in the case of radon (accidental) cluster detection and achieved sufficient results [45]. However, as explained later, the analysis code may need extensions to provide a more reliable tagging of (accidental) clusters in the case of tritium.

6.2.3 Analysis results

Figure 6.2 shows the distribution of the interarrival times for the background afflicted tritium simulation. The major part of the secondary electrons arrives in time frames shorter than $\Delta t_i \leq 1\,\mathrm{s}$ making this a reasonable interarrival time threshold for the cluster detection. Higher interarrival times are more likely coming due to the time difference of the last cluster event of a prior cluster and the first cluster event of the next cluster. In figure 6.3 a background free source is considered that shows a likely interarrival time threshold of $\Delta t = 4\,\mathrm{s}$.

Another important point is to determine the cluster event threshold. Executing the analysis analog to radon, a cluster is made up of at least two secondary electrons. Analyzing the measurement data (or in this case the pseudo data) and setting up a cluster size distribution reveals the common sizes of clusters coming from tritium β-decay.

Using the background smeared pseudo-data from the storage simulation and making a naive assumption of $\Delta t = 0.2\,\mathrm{s}$, as it is done in the radon cluster analysis [45], the detection algorithm gives the cluster size spectra in figure 6.4. The left plot shows the

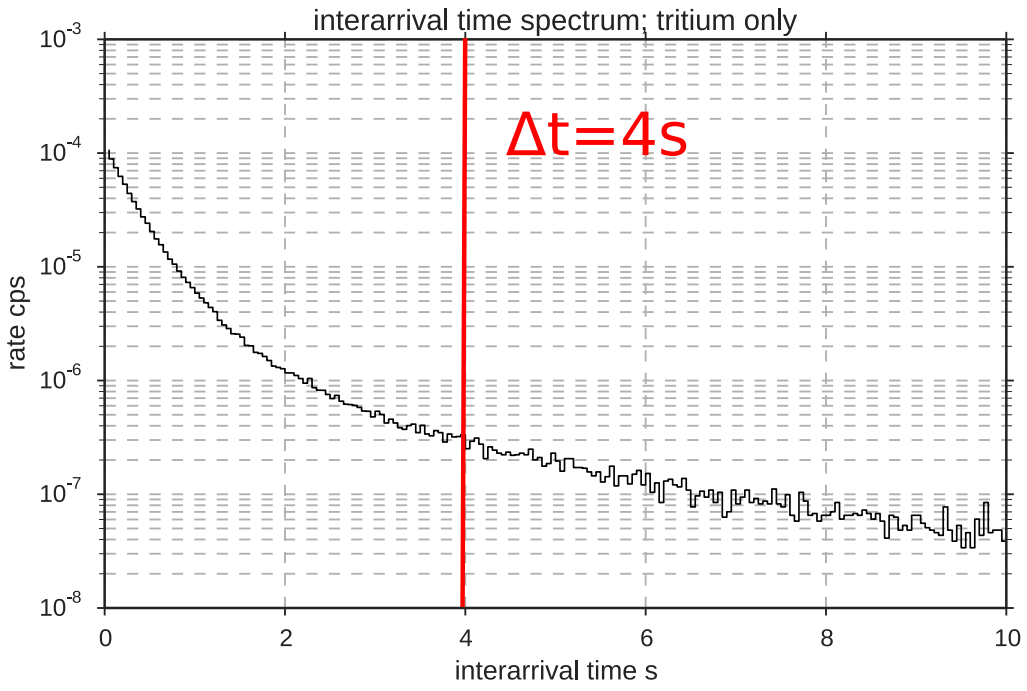

Figure 6.3: Interarrival times of cluster events coming from tritium β-decays and uncorrelated background. Specifying a time frame is not that easy anymore. A time frame of $\Delta t = 4\,\mathrm{s}$ seems accurate.

cluster size distribution without applying an accidental correction. There is a clear peak for clusters with a cluster size of two secondary electrons. Using the accidental correction decreases the amount of clusters with two, three and four cluster events as can be seen on the right side of figure 6.4. The algorithm detected 57857 tritium decays and, thus, about six times more than actually started. The cross-check of the analysis with background free data is given in figure 6.5. The same time threshold applied on the background free data shows that all cluster sizes above ~ 15 are cut off. With about 10^5 detected tritium decays the algorithm found ten times more decays than actually started. Hence, it can be proposed that the considered cluster events appear in large interarrival times.

A possible reason for larger interarrival times for cluster events originating from tritium β-decay is the energy dependent cross-section of the scattering interaction between primary electrons from tritium β-decay and residual gas. It is inversely proportional to the particle energy $E_\mathrm{e} \sim \sigma_{e^- He}(E)^{-1}$ making scattering events of high energy primary particles less likely. During the storage process the primary particle loses its energy by synchrotron radiation. With time its energy decreases, making it more likely to interact with residual gas. After the first scattering event the energy losses are higher and interactions with residual gas occur more often. So the average time between two scattering events decreases as the particle cools down. Choosing a small interarrival time threshold for the detection splits large clusters into several smaller ones resulting in an overestimation of the tritium decays.

A smaller threshold would result in an overestimation of the number of clusters as single clusters split up into several. Choosing a too large threshold results in an underestimation of the cluster rate as two or more clusters are then considered as one larger cluster. Another problem that arises is the case for accidental cluster detection. A small threshold does not only split one single cluster into several but also increases the amount of accidental clusters consisting of uncorrelated background. The accidental detection algorithm would then not

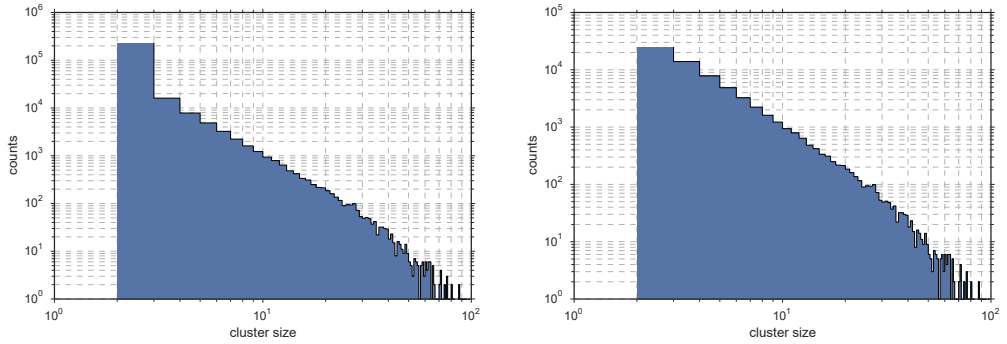

Figure 6.4: Uncorrected and corrected cluster size distribution determined with $\Delta t = 0.2\,\mathrm{s}$. Left: The cluster size spectrum without an accidental correction shows high numbers of clusters that are made up by two cluster events. **Right:** Applying an accidental correction reduces the number of clusters with a multiplicity of two (three and four).

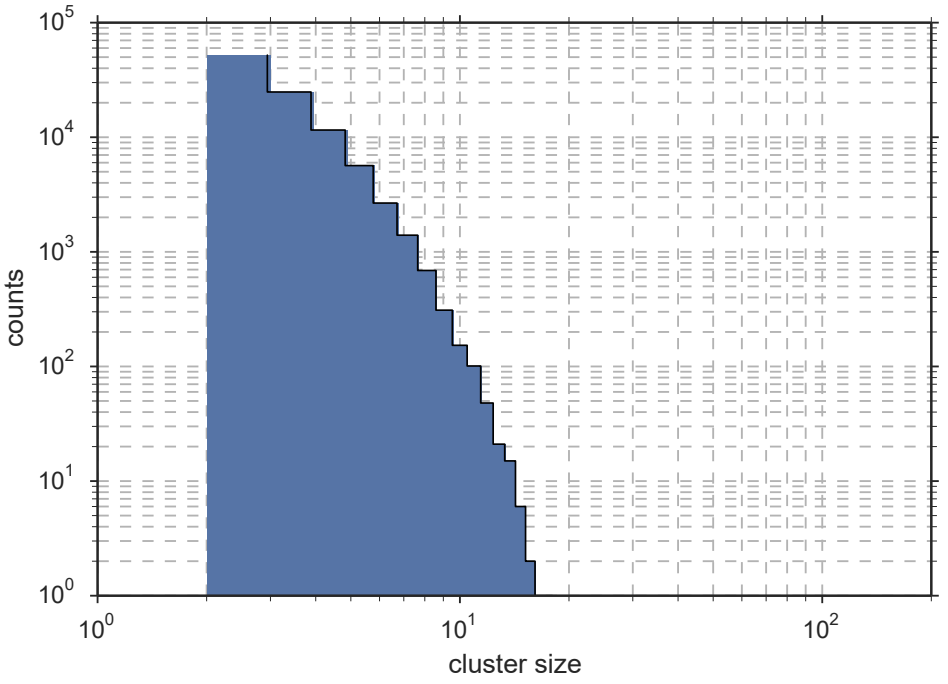

Figure 6.5: Cluster size distribution of background-free data with $\Delta t = 0.2\,\mathrm{s}$. Choosing a small cluster time frame as done with radon results in a high number of small clusters. Larger clusters are cut off.

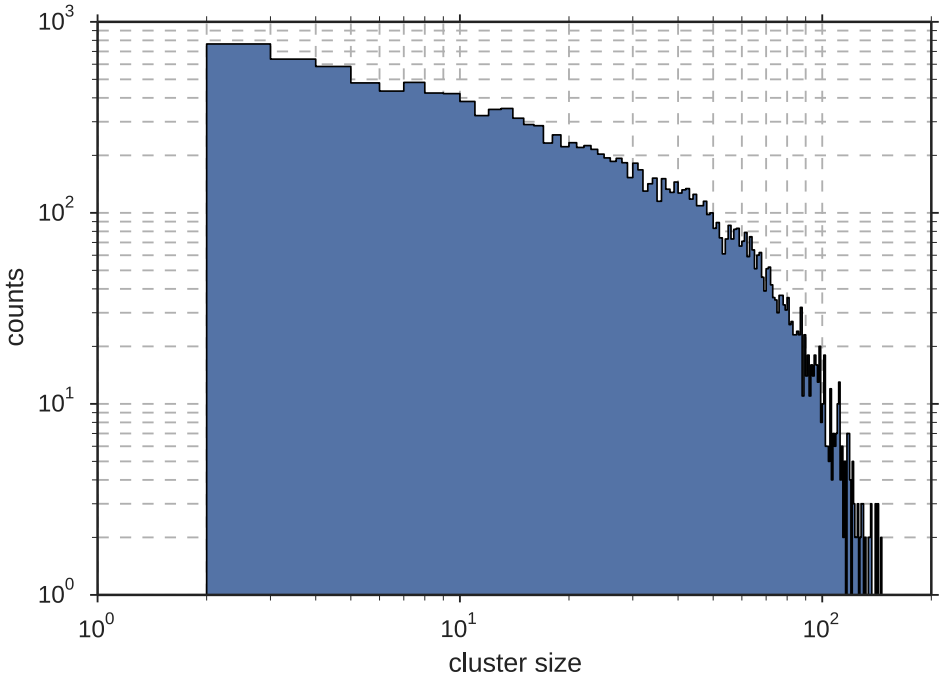

Figure 6.6: Cluster size distribution of background free data with $\Delta t = 4\,\mathrm{s}$. Increasing the time threshold leads to counts of higher cluster sizes. The algorithm counts about 14„00 tritium decays.

only decrease the amount of accidental clusters but also the amount of clusters originated from tritium β-decay. That is because more and more counted clusters would fulfill the requirement for uncorrelated background given in equation 6.3. On the other hand a too large threshold would not only add several clusters into one larger cluster but also add single events in those larger clusters. It follows that the time series for the cluster series decreases and the algorithm would not be able to detect all accidental hits. Understanding the physics of scattering events and generation of secondary electrons is crucial to achieve reliable parameters for the analysis.

So the first step is to increase the time threshold to $\Delta t = 4\,\mathrm{s}$ according 6.3. The plot for this parameter is given in figure 6.6 and shows that larger cluster sizes are now counted as well as the shorter ones. With about 14000 counted tritium decays the error is much smaller than before but still higher than the input. Increasing the threshold once again to a very high time difference of $\Delta t = 60\,\mathrm{s}$ shows no greater changes of the shape of the cluster size distribution (see figure 6.7) but with about 7800 clusters counts too less tritium decays. Considering the preparatory simulations, where about $80-85\%$ of particles reached the detector, the detection limit seems plausible. Indeed, the value of 7800 clusters is approached by setting a greater time threshold than $\Delta t > 15\,\mathrm{s}$, e.g. a threshold of $\Delta t = 20\,\mathrm{s}$ counted 7872 clusters in total.

So in general higher threshold times seem more reliable in detecting tritium decays. However, looking back at the simulation data with applied uncorrelated background (in figure 6.4) increasing only the time difference does not suffice as the impact of the uncorrelated background is too large. One possibility would be to increase the time threshold and also increase the value for the cluster size threshold. This would cut off all clusters with cluster sizes smaller than the threshold but also minimize the impact of the uncorrelated background. In table 6.1 once again different detection counts are shown.

Table 6.1: Number of cluster detections.

detection type	tritium decays
input	10 000
expected	$\sim$ 7 800
clusters detected	274 622
accidentals detected	216 765
corrected clusters	57 857

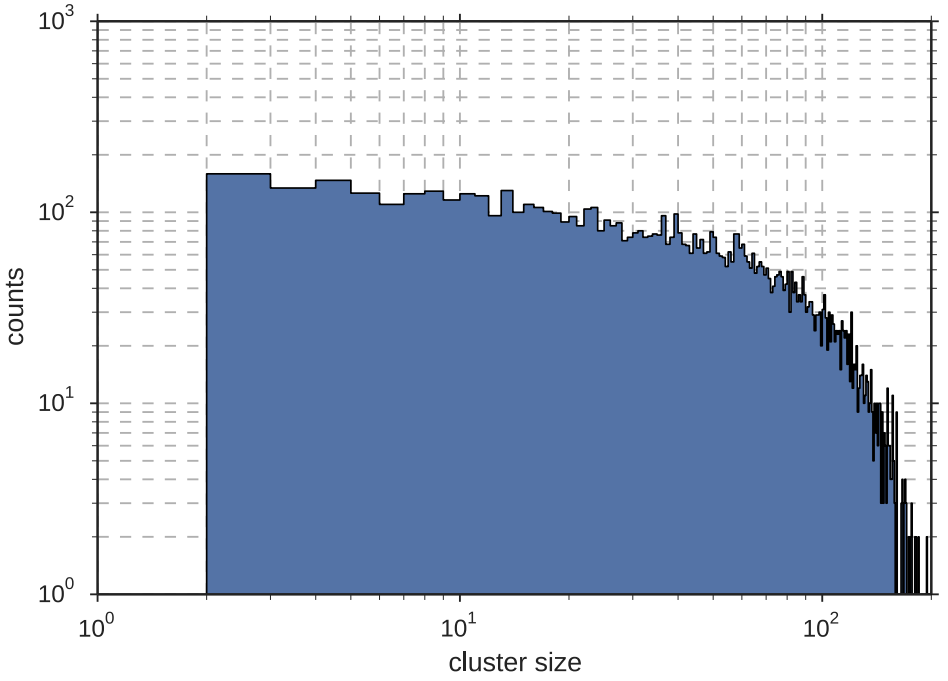

Figure 6.7: Cluster size distribution of background free data with $\Delta t = 60\,\mathrm{s}$. Increasing the interarrival time threshold to one minute has nearly no influence on the shape of the cluster size distribution. But the cluster count decreases to $\sim$ 7800 tritium decays.

As the analysis code only focuses on arrival times this result is somewhat expected but still too far off to be acceptable. Beside analyzing arrival times of cluster events it is also a possibility to look at each pixel of the detector that is hit by the particles. Cluster events that belong together should arrive in a ring pattern (see chapter 5). Improving the analysis code by including a spacial analysis of events likely to provide a more precise cluster detection.

Another point is the assumed decay rate of tritium and the rate of the uncorrelated background that is about $2 \cdot 10^3$ times higher than the decay rate of tritium. The signal of the uncorrelated background heavily worsens the analysis and, thus, the detection of tritium decays. Beside decreasing the background rate, which would take too long and would also be not that easy to do, it is possible to increase the spectrometer pressure. With a higher pressure the probability of scattering events between primary electrons and residual gas is increased and more secondary electrons reach the detector in shorter time intervals, hence, improving the signal. Additional simulations have to be done to verify these approaches.

6.2.3.1 Number of secondary electrons and detection ratio

Another way of measuring the decay rate of tritium in the PS is to compare the detector signal before and afterwards the valve is opened to the CPS. The average number of secondary electrons that are produced by a primary electron and reach the detector is needed to calculate the decay rate. The difference of both signals can be explained by the additional tritium decays in the PS after the valve was opened. This method does not rely on sophisticated analysis code, but solely uses the signal at the focal-plane detector.

The storage simulation shows that a tritium decay results in average in 120 low energy electrons that are generated in the PS. Out of this number about 37 electrons reach the detector. With a detection ratio of only 30.65% the simulated ratio is, therefore, far off the detection ratio that was estimated with the preparatory simulations (see chapter 5). An explanation could be, that all particles in the preparatory simulations started in the flux tube of the PS. Everything inside the flux volume is theoretically detectable. In the storage simulation, however, tritium decays started in the PS tank. It could be the case that many secondary electrons that were generated outside of the flux tube had no chance to reach the detector and, thus, did not appear in the data set.
Another point is the asymmetric potential configuration of the PS. Due to the more negative upstream full-metal cone electrode, primary electrons are more likely to leave the PS. Prior to thermalization those primary electrons can then be stored in the MS rather than directly reaching the detector. Secondary electrons that are generated by the cool-down process of these primaries in the MS do not possess the same magnitude of energy as the secondary electrons that are generated in the PS due to the zero potential configuration of the MS. For not being in the region of interest these secondary electrons, that are created in the MS, are considered as background and not counted in the cluster search algorithm. In this storage simulation about 58% of all secondary electrons generated were terminated due to having a smaller total energy $E_{\mathrm{tot}} = 15.6\,\mathrm{keV}$ than allowed. Adding up both fractions would lead to about the same detection ratio as estimated in the preparatory simulations.

6.3 Discussion of results

One way to detect tritium decays in the PS and in this way obtain information about the functionality of the CPS in future experiments is to identify characteristic event clusters that are generated in this context. Distinguishing between clusters originating from actual tritium decays and accidental clusters from background processes is of utmost importance.

In this chapter the analysis code so far compares only interarrival times of cluster events and misses the targeted number of tritium decays by a factor of six. To increase the detection efficiency it is recommended to utilize the spatial characteristics of stored particle induced background in addition to the temporal structure, i.e. to use the ring-like event pattern described in chapter 5. Spatial signature will improve the results as well as varying the interarrival time threshold and the cluster size threshold. As the interarrival times of secondary electrons are larger than assumed, the impact of uncorrelated background events is higher when setting higher time thresholds. This can be (partly) countered by setting the cluster size threshold to a higher value, however, the effect on the accidental detection algorithm needs to be considered. By increasing the pressure and, thus, the scattering probability of primary electrons with residual gas, the signal of secondary electrons is improved. Hence, a more effective analysis is allowed.
The detection of tritium decays in the PS by only observing the signal of secondary electrons is also possible. While the asymmetric potential configuration of the PS electrodes not only leads secondary electrons towards the MS but also primary electrons, the overall signal rate decreased as secondary electrons generated in the MS are outside the region of interest.

Setting the PS electrode potentials back to a symmetric configuration or decreasing the difference between the full-metal cone electrodes of the PS will likely increase the signal again and improve that arrival rate of secondary electrons.

Considering the tritium rate that was calculated in chapter 5 and the signal to noise ratio, the feasibility of this detection method is given. However, the analysis code needs additional detection criteria for higher cluster counting precision. All in all, checking the functionality of the CPS by counting tritium β-decays in the PS is a possible approach and can be considered later during experimental runs.

7. Ion simulation

Not only neutral tritium molecules can generate background through decays, but also ionized particles. As these ions are guided by the magnetic field, pumping them out is rather ineffective. This chapter discusses the ionization of particles, their behavior and the background emerging from these particles. Subsequently, an ion blocking method is investigated in the context of this work. This chapter concludes with a summary of the achieved results.

7.1 Ion generation

The WGTS provides the tritium that is needed for the KATRIN experiment. The tritium exists as molecule of two tritium atoms. The β-decay that generates the electrons, that are to be measured, creates the ionized molecules. The reaction is ($^3_1\mathbf{H}_2 = \mathbf{T_2}$)

$$\mathbf{T}_2 \longrightarrow {}^3_2\mathbf{HeT}^+ + e^- + \bar{\nu}_e \quad . \tag{7.1}$$

Due to the relatively high density in the WGTS and with $\mathbf{T}_2$ being the dominant source of tritium (there also exist hydrogen-tritium molecules), those reactions occur rather frequently. $\mathbf{T}_2$ can decay to an excited ${}^3_2\mathbf{HeT}^+$ molecule that can split into ${}^3_2\mathbf{He}^+ + \mathbf{T}$ or $\mathbf{T}^+ + {}^3_2\mathbf{He}$. These two ions are called *primary ions* as they are generated directly through β-decay. Another source of ions is via inelastic scattering of molecules with primary electrons that. Possible reactions are

$$e^- + \mathbf{T_2} \longrightarrow 2e^- + \mathbf{T_2} \tag{7.2}$$

and

$$e^- + \mathbf{T_2} \longrightarrow 2e^- + \mathbf{T} + \mathbf{T}^+ \quad . \tag{7.3}$$

Ions generated from inelastic scattering are called *secondary ions*. The reaction in equation 7.2 makes up 96% of all occurring reaction and is the dominant one. The reaction in equation 7.3 makes up the rest 4% [49]. With high densities, nearly all of the ${}^3_2\mathbf{He}^+$ ions convert to $\mathbf{T}_3^+$ due to the chemical reaction

$${}^3_2\mathbf{HeT}^+ + \mathbf{T}_2 \longrightarrow {}^3_2\mathbf{He} + \mathbf{T}_3^+ \quad . \tag{7.4}$$

Other reactions that produce $\mathbf{T}_3^+$ are

$$
\begin{aligned}
{}^3_2\mathbf{He}^+ + \mathbf{T}_2 &\longrightarrow {}^3_2\mathbf{He} + \mathbf{T} + \mathbf{T}^+ \quad , && (7.5)\\
{}^3_2\mathbf{He}^+ + \mathbf{T}_2 &\longrightarrow {}^3_2\mathbf{He} + \mathbf{T}_2^+ \quad , && (7.6)\\
\mathbf{T}_2^+ + \mathbf{T}_2 &\longrightarrow \mathbf{T} + \mathbf{T}_3^+ \quad . && (7.7)
\end{aligned}
$$

Negative charged ions are mainly created by electron scattering with tritium molecules (dissociative attachment)

$$e^- + \mathbf{T}_2 \longrightarrow \mathbf{T} + \mathbf{T}^- \quad . \tag{7.8}$$

As those ions have only one way to be created, they are assumed to make up 2% of all ions [50].

7.1.1 Molecular ions

With chemical reactions it is possible to create molecule clusters of the form of $\mathbf{T}^+_{2n+1}$. This happens by the following chemical reactions

$$\mathbf{T}^+ + \mathbf{T}_2 + \mathbf{T}_2 \longrightarrow \mathbf{T}_2 + \mathbf{T}_3^+ \quad , \tag{7.9}$$

and

$$\mathbf{T}_3^+ + \mathbf{T}_2 + \mathbf{T}_2 \longrightarrow \mathbf{T}_2 + \mathbf{T}_5^+ \quad . \tag{7.10}$$

Especially several repetitions of the equation 7.10 creates heavier tritium cluster molecules in the WGTS:

$$\mathbf{T}^+_{2n+1} + \mathbf{T}_2 + \mathbf{T}_2 \longrightarrow \mathbf{T}_2 + \mathbf{T}^+_{2n+3} \quad . \tag{7.11}$$

So besides $\mathbf{T}_3^+$ also $\mathbf{T}_5^+$ and $\mathbf{T}_7^+$ make up the positive ions that appear in the WGTS. Due to high interaction cross-sections and low mean free paths ($\sim 1\,\mathrm{mm}$), those reactions take place rather quickly [50].

7.1.2 Recombination of ions

Positive charged ions can be neutralized by recombining with slow electrons. The neutral molecules are then no longer guided by the magnetic field and can be removed by vacuum pumps. The recombination rate R is described as

$$R = \alpha \cdot \rho_{\mathrm{ion}} \rho_{\mathrm{electron}} \quad , \tag{7.12}$$

with α as the recombination coefficient, ρ_{ion} the density of ions and ρ_{electron} the density of electrons. Values for the recombination coefficients are large and can range from $10^{-8}\,\mathrm{cm^3 s^{-1}}$ to $10^{-5}\,\mathrm{cm^3 s^{-1}}$. With higher tritium cluster molecule sizes the recombination coefficient increases [50]. In case of $\mathbf{T}_3^+$ the recombination reaction with an electron is

$$\mathbf{T}_3^+ + e^- \longrightarrow \mathbf{T}_2 + \mathbf{T} \quad . \tag{7.13}$$

It is also possible for positive charged ions to recombine with negative charged ions. The reaction for $\mathbf{T}^+$ is

$$\mathbf{T}^+ + \mathbf{T}^- \longrightarrow \mathbf{T} + \mathbf{T} \tag{7.14}$$

and for $\mathbf{T}_3^+$ it is

$$\mathbf{T}_3^+ + \mathbf{T}^- \longrightarrow \mathbf{T}_2 + \mathbf{T} + \mathbf{T} \quad , \tag{7.15}$$
$$\mathbf{T}_3^+ + \mathbf{T}^- \longrightarrow \mathbf{T} + \mathbf{T} + \mathbf{T} + \mathbf{T} \quad . \tag{7.16}$$

7.1.3 Ion currents

Due to processes mentioned above, about $2 \cdot 10^{12}$ tritium ions are generated per second in the WGTS. Considering chemical reactions and recombinations rates, the total flux of positive ions from the WGTS towards the transport section is assumed to be about $2 \cdot 10^{11}\,\mathrm{s}^{-1}$. For negative ions ($\mathbf{T}^-$) the rate is $2 \cdot 10^{10}\,\mathrm{s}^{-1}$.

Table 7.1: Ion currents at the end of the WGTS. Data taken from [51].

ion	currents in nA
$\mathbf{T}_3^+$	19.0
$\mathbf{T}_5^+$,$\mathbf{T}_7^+$, etc.	6.5
$\mathbf{T}^+$	1.0
$\mathbf{He}^+$	0.25
$\mathbf{T}^-$	2.0

The currents of ions at the detector-side end of the WGTS is shown in table 7.1. As mentioned, the dominant ion source is made up by $\mathbf{T}_3^+$ and higher molecule clusters.

7.2 Impact of ions

The energy of ions is mainly thermal energy. In close space that can lead to a high-density plasma that increases the space charge of the WGTS. Plasma instabilities could also have an effect on the energy of β-electrons that are meant to be measured for the neutrino rest mass. Another point is, primary electrons from those ions possess different endpoint energies than the ones coming from tritium β-decay and can impact the measurement of the neutrino-mass in a negative way [37].

If the PS is run on negative potential, negative charged ions can not reach the spectrometer section and are reflected back and forth in the transport section. Positive charged ions, however, are able to reach the detector and can cause a tritium contamination of the spectrometers. That would be fatal for the experiment and should be avoided by all means as ion decays in the spectrometers and/or ionization of other molecules would make up a non-negligible background that hugely worsens the measurement data.

7.3 Ion blocking

A major part of the ions recombines with slow electrons and neutralizes. Those neutralized ions can be removed by vacuum pumps, however, the rate of remaining ions is still non-negligible and has to be removed by additional methods.

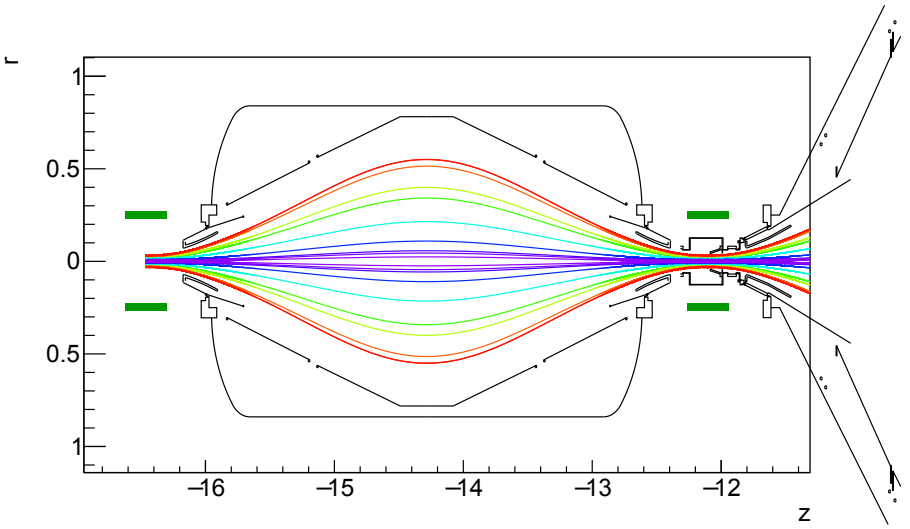

Figure 7.1: Simulated tracks of positive charged ions through PS without potential. Ions follow the magnetic field lines, enter the MS and are able to generate a background signal.

In the content of this work, the ion blocking in the PS was analyzed in detail. Further methods like the $\vec{E} \times \vec{B}$-drift are discussed in the diploma thesis of Stefan Reimer [49] and in [37].

As negative ions can not reach the PS due to negative blocking potentials, they have to be removed in the transport section and are not considered further in this case. Positive ions, however, can reach the spectrometers by following the magnetic field lines. Figure 7.1 shows the track of ten $\mathbf{T}_3^+$ ions started at the beginning of the PS with no PS electrode potentials set. With a magnetic field generated by the air coils as given in table 7.2 all ions are able to enter the MS.
To avoid that, all PS electrodes were set on −200 V and are displayed in table 7.3. The simulation was done with $\mathbf{T}_3^+$ with 10^5 ions starting at the beginning of the PS on a disk surface which corresponds to the beam tube.

Table 7.2: LFCS setting for ion tracking simulation. The currents of the air coil system of the MS are set on the highest possible values.

air coil	current in A
1 & 2	100.0
3-11	175.0
12 & 13	100.0
14	70.0

With a nonzero potential configured for the PS, nearly all ions collide with the spectrometer hull and therefore can not enter the MS. Positive ions are accelerated by the negative potential and lose their adiabatic guidance. They result in a chaotic movement and at one point fly against the spectrometer hull. Out of 10^5 ions only 0.07% were able to enter the MS. Increasing the voltage from −200 V to −1 kV, no ion was able to enter the MS at all. Ions that entered the MS with a PS potential of −200 V had very small distances to the z-axis.

Figure 7.2 shows the simulation of ions with a negative potential set in the PS. Therefore, this configuration successfully permits ions from entering the MS. A better view of a single positive charged ion is given in figure 7.3. The movement of the ion is chaotic and after some oscillations the particle hits the spectrometer hull.

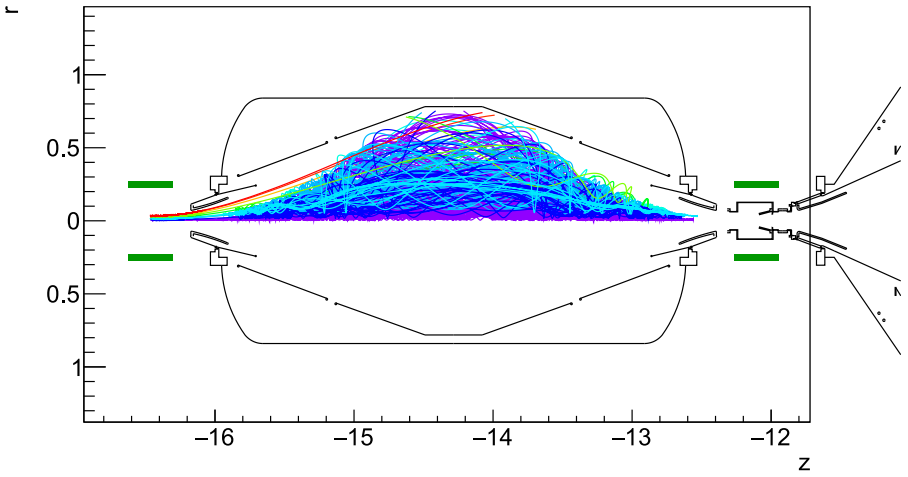

Figure 7.2: Simulated tracks of positive charged ions through the PS with a potential of −200 V. Ions are no longer guided adiabatically in the PS and end up hitting the spectrometer hull.

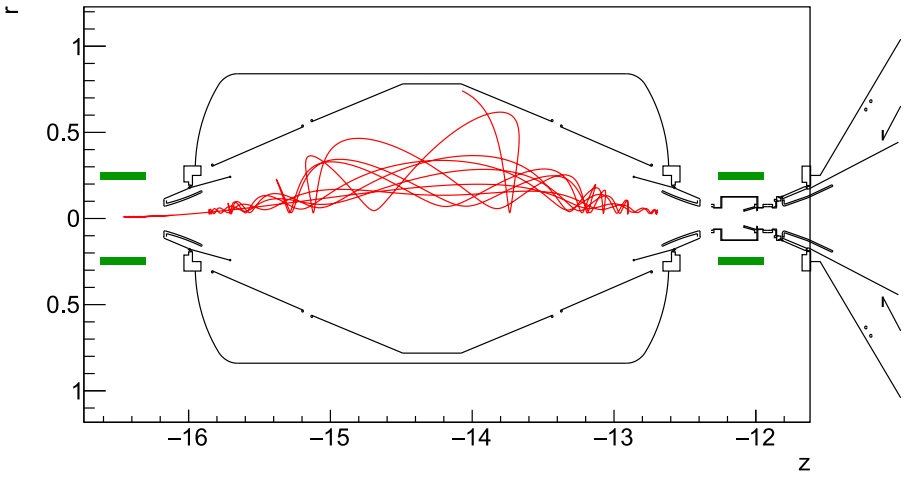

Figure 7.3: Simulation of a single positive ion through PS with a potential of −200 V. Chaotic movement of a $\mathbf{T}_3^+$ ion in the PS. After some oscillations the ion ends up colliding with the spectrometer hull.

Table 7.3: PS potential configuration for ions.

electrode	potential in V
hull electrode	-200.0
wire electrode	-200.0
full-metal electrodes (both)	-200.0

Further increasing the potential, i.e. to 1 kV, successfully prevented all ions from entering the MS.

7.4 Summary

Ions occur mainly as charged tritium molecules $\mathbf{T}_3^+$ and higher tritium cluster like $\mathbf{T}_5^+$, $\mathbf{T}_7^+$ and higher. Negative charged tritium $\mathbf{T}^-$ makes only up to 2% of all ions. The source of these ions is the tritium β-decay, ionization of β-electrons and chemical reactions. Inelastic electron tritium scattering generates positive and negative charged ions that are called secondary ions.
Ions are guided by the magnetic field to the spectrometer and therefore not efficiently removed by vacuum pumps. A large fraction of ions is able to recombine with slow electrons from the WGTS and neutralizes. Neutral molecules are no longer guided by the magnetic field and, thus, are able to be removed by vacuum pumps. Different approaches have to be carried out to further reduce the ion flow. Setting the PS electrodes on negative potential blocks all negative charged ions from entering the spectrometer section. Positive ions are accelerated and lose their adiabatic guidance. Only a small amount of ions were able to reach the MS with a PS potential $-200\,\mathrm{V}$. Higher voltages for example $-1\,\mathrm{kV}$ successfully blocked all ions.

The benefit of this method is that it reliably blocks almost all ions that enter the PS. The problem however is that ions can no longer be monitored. An eventual neutralization of those ions in the PS remains unobserved, thus, making it impossible to tell whether neutral tritium atoms or molecules (that were ionized before) are able to enter the MS.

8. Conclusion

The **Ka**rlsruhe **Tri**tium **N**eutrino (KATRIN) experiment aims to probe the mass of the electron antineutrino in a model-independent way with a sensitivity of $m_\nu = 200\,\mathrm{meV/c^2}$ (90% C.L.). The beamline of the KATRIN experiment begins with the rear section and the windowless gaseous tritium source. The transport section that consists of the differential pumping section and the cryogenic pumping section follows until the pre-spectrometer, main-spectrometer and the detector finish the beamline. Beside the electron transport, the tritium reduction is the second key task of the transport section. Only few molecules are able to migrate into the pre-spectrometer as the tritium flux is reduced by many orders. The tritium β-decay generates primary electrons that are magnetically trapped in the volume of the pre-spectrometer with typical energies on the order of a few keV. Via subsequent ionization of residual gas molecules, the primary trapped electrons produces a cluster of several secondary electrons which can be transported and detected at the focal-plane detector. A simulation of these electrons in a realistic setup allows a better understanding of the tritium activity in the pre-spectrometer.

In this thesis a feasibility study was done for detecting tritium β-decay in the pre-spectrometer and, thus, identifying the efficiency of the cryogenic pumping-section. Starting with secondary electron simulations, different parameters were checked on to find the ideal configuration for the simulation of stored particles. For a high signal to noise ratio of secondary electrons, the electromagnetic configuration of the spectrometer and detector section was modified. The analysis of the simulation data showed the effect of the energy dependent interaction cross-section of tritium β-electrons with residual gas that is inversely proportional to the particle energy, thus, making scattering event of high energy β-electrons less likely. After energy-loss processes like synchrotron radiation the probability of a scattering event increases and explains the time difference between the secondary electrons of a single cluster.
Considering (uncorrelated) background, choosing a favorable time frame between secondary electrons reaching the detector is made more difficult as background events affect the cluster count and, thus, distort the number of counted tritium decays.

A possible way to further refine the analysis algorithm can be done by adding spatial information of the secondary electrons. Secondary electrons that belong to the same cluster hit on the detector in a ring shape. Filtering false hits by checking the pixels should improve the analysis and lessen the number of accidental detections.
Another way to improve the detection signal is to increase the cluster size threshold. By this means, the influence of uncorrelated background is decreased but other than that all clusters with a size lower than the threshold are cut off. Another downside of this method is the less effective accidental cluster search algorithm. So all in all, a balance of both consequences is needed to achieve optimal conditions and, thus, a better cluster detection.

Without using the cluster detection method, a clear secondary electron signal may suffice

to deduce the rate of tritium decay in the pre-spectrometer. It is therefore necessary to guide most of the generated secondary electrons to the detector and, thus, improve the signal. By using an asymmetric potential configuration of the pre-spectrometer, where the upstream cone electrode was set more negative than the downstream cone electrode, secondary electrons were more likely guided towards the detector. In the end it also caused primary electrons to leave the pre-spectrometer, generating secondary electrons outside of the region of interest and resulting in an overall lower signal. With decreasing the potential difference of the pre-spectrometer cone electrodes a more improved signal can be achieved. Further simulations are needed to confirm that.

To make a statement on the functionality of the cryogenic pumping-section by detecting single tritium β-decays in the pre-spectrometer requires further refinement of the analysis. The current cluster detection algorithm with subsequent accidental cluster detection counted six times more tritium decays than the input. With more evaluated parameters, i.e. considering detector pixel, the counting of cluster sizes can be made more precise. Summarized, the described method of testing the functionality of the cryogenic pumping section is possible by detecting tritium β-decay in the pre-spectrometer, but needs more sophisticated analysis algorithms to lower the impact of other background sources.

The case for ionized (tritium) molecules is a bit different than neutral molecules. As ions are guided by the magnetic field, vacuum pumps do not affect them and, thus, additional methods have to be set up to prevent them causing another source of background. Unlike negative ions, that are not able to enter the spectrometers due to the negative electrode potentials, positive ions can enter the spectrometers and decay there or ionize residual gas. By setting higher electrode potentials, the trajectory of those positive ions is chaotic and leads to a collision with the spectrometer hull. Hence, the background of positive ions is minimized but a monitoring of those ions is then no longer possible.

Bibliography

[1] J. Chadwick, "Intensitätsverteilung im magnetischen spektrum der β-strahlen von radium b+c," *Verhandl. Dtsc. Phys. Ges.*, vol. 16, p. 383, 1914.

[2] W. Pauli, "Offener brief an die gruppe der radioaktiven bei der gauvereins-tagung zu tübingen," *datiert*, 1930, "[Online; accessed 22-August-2016]".

[3] J. Chadwick, "The existence of a neutron," in *Proceedings of the Royal Society of London A: Mathematical, Physical and Engineering Sciences*, vol. 136, no. 830. The Royal Society, 1932, pp. 692–708.

[4] E. Fermi, "Versuch einer theorie der β-strahlen. i," *Zeitschrift für Physik*, vol. 88, no. 3-4, pp. 161–177, 1934.

[5] H. Bethe and R. Peierls, "The'neutrino'," *Nature*, vol. 133, no. 3362, p. 532, 1934.

[6] C. L. Cowan, Jr., F. Reines, F. B. Harrison, H. W. Kruse, and A. D. McGuire, "Detection of the Free Neutrino: A Confirmation," *Science*, vol. 124, pp. 103–104, Jul. 1956.

[7] G. Danby, J. Gaillard, K. Goulianos, L. Lederman, N. Mistry, M. Schwartz, and J. Steinberger, "Observation of high-energy neutrino reactions and the existence of two kinds of neutrinos," *Physical Review Letters*, vol. 9, no. 1, p. 36, 1962.

[8] K. A. Olive *et al.*, "Review of Particle Physics," *Chin. Phys.*, vol. C38, p. 090001, 2014.

[9] M. L. Perl, G. Abrams, A. Boyarski, M. Breidenbach, D. Briggs, F. Bulos, W. Chinowsky, J. Dakin, G. Feldman, C. Friedberg *et al.*, "Evidence for anomalous lepton production in e+- e- annihilation," *Physical Review Letters*, vol. 35, no. 22, p. 1489, 1975.

[10] K. Kodama *et al.*, "Observation of tau neutrino interactions," *Phys. Lett.*, vol. B504, pp. 218–224, 2001.

[11] O. Adriani, M. Aguilar-Benitez, S. Ahlen, H. Akbari, J. Alcaraz, A. Aloisio, G. Alverson, M. Alviggi, G. Ambrosi, Q. An *et al.*, "Determination of the number of light neutrino species," *Physics Letters B*, vol. 292, no. 3, pp. 463–471, 1992.

[12] J. N. Bahcall, M. H. Pinsonneault, and G. J. Wasserburg, "Solar models with helium and heavy-element diffusion," *Rev. Mod. Phys.*, vol. 67, pp. 781–808, Oct 1995. [Online]. Available: http://link.aps.org/doi/10.1103/RevModPhys.67.781

[13] J. N. Bahcall, A. M. Serenelli, and S. Basu, "New solar opacities, abundances, helioseismology, and neutrino fluxes," *The Astrophysical Journal Letters*, vol. 621, no. 1, p. L85, 2005. [Online]. Available: http://stacks.iop.org/1538-4357/621/i=1/a=L85

[14] R. Davis, D. S. Harmer, and K. C. Hoffman, "Search for neutrinos from the sun," *Phys. Rev. Lett.*, vol. 20, pp. 1205–1209, May 1968. [Online]. Available: http://link.aps.org/doi/10.1103/PhysRevLett.20.1205

[15] B. Pontecorvo, "Inverse beta processes and nonconservation of lepton charge," *Sov. Phys. JETP*, vol. 7, pp. 172–173, 1958, [Zh. Eksp. Teor. Fiz.34,247(1957)].

[16] Z. Maki, M. Nakagawa, and S. Sakata, "Remarks on the unified model of elementary particles," *Progress of Theoretical Physics*, vol. 28, no. 5, pp. 870–880, 1962. [Online]. Available: http://ptp.oxfordjournals.org/content/28/5/870.abstract

[17] J. Iizuka, T. Kitabayashi, Y. Minagawa, and M. Yasue, "Parametrization of Pontecorvo–Maki–Nakagawa–Sakata mixing matrix based on CP-violating bipair neutrino mixing," *Mod. Phys. Lett.*, vol. A30, no. 05, p. 1550019, 2015.

[18] A. Hime, "Results from the Sudbury Neutrino Observatory," in *APS Four Corners Section Meeting Abstracts*, Nov. 2001.

[19] Y. Takeuchi, "Results from super-kamiokande," *Nuclear Physics B - Proceedings Supplements*, vol. 229, pp. 79 – 84, 2012. [Online]. Available: http://www.sciencedirect.com/science/article/pii/S0920563212002307

[20] P. Anselmann *et al.*, "Gallex solar neutrino observations. the results from gallex i and early results from gallex ii," *Physics Letters B*, vol. 314, no. 3, pp. 445 – 458, 1993. [Online]. Available: http://www.sciencedirect.com/science/article/pii/037026939391264N

[21] X. Qian and P. Vogel, "Neutrino mass hierarchy," *Progress in Particle and Nuclear Physics*, vol. 83, pp. 1 – 30, 2015. [Online]. Available: http://www.sciencedirect.com/science/article/pii/S0146641015000307

[22] S. F. King and C. Luhn, "Neutrino Mass and Mixing with Discrete Symmetry," *Rept. Prog. Phys.*, vol. 76, p. 056201, 2013.

[23] J. Lesgourgues and S. Pastor, "Neutrino mass from Cosmology," *Adv. High Energy Phys.*, vol. 2012, p. 608515, 2012.

[24] ——, "Neutrino cosmology and Planck," *New J. Phys.*, vol. 16, p. 065002, 2014.

[25] K. Zuber, "Experimental neutrino physics," *Int. J. Mod. Phys.*, vol. A20, p. 2895, 2005.

[26] J. S. Schwarz, "The detector system of the KATRIN experiment - implementation and first measurements with the spectrometer," Ph.D. dissertation, Karlsruher Institut für Technologie (KIT), 2014. [Online]. Available: http://nbn-resolving.org/urn:nbn:de:swb:90-427724

[27] S. M., "Accurate calibration of the Raman system for the Karlsruhe Tritium Neutrino Experiment," *doctoral thesis*, 2013.

[28] S. R. Elliott and P. Vogel, "Double beta decay," *Ann. Rev. Nucl. Part. Sci.*, vol. 52, pp. 115–151, 2002.

[29] M. Agostini *et al.*, "Results on Neutrinoless Double-β Decay of ^{76}Ge from Phase I of the GERDA Experiment," *Phys. Rev. Lett.*, vol. 111, no. 12, p. 122503, 2013.

[30] S. R. Elliott and P. Vogel, "Double beta decay," *Ann. Rev. Nucl. Part. Sci.*, vol. 52, pp. 115–151, 2002.

[31] G. Drexlin, V. Hannen, S. Mertens, and C. Weinheimer, "Current Direct Neutrino Mass Experiments," *Advances in High Energy Physics*, vol. vol. 2013, p. 39, 2013.

[32] N. Wandkowsky, "Study of background and transmission properties of the KATRIN spectrometers," Ph.D. dissertation, Karlsruher Institut für Technologie (KIT), 2013. [Online]. Available: http://digbib.ubka.uni-karlsruhe.de/volltexte/1000036631

[33] S. Groh, "Untersuchung von uv-laser induziertem untergrund am KATRIN vorspektrometer," Diploma Thesis, Karlsruher Institut für Technologie (KIT), 2010. [Online]. Available: http://www.katrin.kit.edu/publikationen/dth-groh.pdf

[34] F. Harms, "Characterization and minimization of background processes in the katrin main spectrometer," Ph.D. dissertation, Karlsruher Institut für Technologie (KIT), 2015. [Online]. Available: http://nbn-resolving.org/urn:nbn:de:swb:90-500274

[35] KATRIN collaboration, "KATRIN design report," *FZKA scientific report*, vol. 7090, 2005. [Online]. Available: http://bibliothek.fzk.de/zb/berichte/FZKA7090.pdf

[36] M. Babutzka, "Design and development for the rearsection of the katrin experiment," Ph.D. dissertation, Karlsruher Institut für Technologie (KIT), 2014, karlsruhe, KIT, Diss., 2014. [Online]. Available: http://digbib.ubka.uni-karlsruhe.de/volltexte/1000045598

[37] M. Klein and F. Glück, "Tritium ion blocking and detection in the katrin experiment," 2015.

[38] F. M. Fränkle, "Background investigations of the KATRIN pre-spectrometer," Ph.D. dissertation, Karlsruher Institut für Technologie (KIT), 2010. [Online]. Available: http://nbn-resolving.org/urn:nbn:de:swb:90-193929

[39] J. F. Amsbaugh *et al.*, "Focal-plane detector system for the KATRIN experiment," *Nucl. Instrum. Meth.*, vol. A778, pp. 40–60, 2015.

[40] S. Groh, "Modeling of the response function and measurement of transmission properties of the KATRIN experiment," Ph.D. dissertation, Karlsruher Institut für Technologie (KIT), 2015. [Online]. Available: http://nbn-resolving.org/urn:nbn:de:swb:90-465464

[41] F. Glück, "Runge-kutta method for numerical solution of differential equation system," *internal KATRIN document*, 2008.

[42] F. Gluck, "Axisymmetric magnetic field calculation with zonal harmonic expansion," *Progress In Electromagnetics Research B*, vol. 32, pp. 351–388, 2011.

[43] S. Mertens, G. Drexlin, F. Fränkle, D. Furse, F. Glück, S. Görhardt, M. Hötzel, W. Käfer, B. Leiber, T. Thümmler, N. Wandkowsky, and J. Wolf, "Background due to stored electrons following nuclear decays in the {KATRIN} spectrometers and its impact on the neutrino mass sensitivity," *Astroparticle Physics*, vol. 41, pp. 52 – 62, 2013. [Online]. Available: http://www.sciencedirect.com/science/article/pii/S0927650512001892

[44] N. Wandkowsky, "Study of background and transmission properties of the KATRIN spectrometers," Ph.D. dissertation, Karlsruher Institut für Technologie (KIT), 2013. [Online]. Available: http://digbib.ubka.uni-karlsruhe.de/volltexte/1000036631

[45] J. S. Schwarz, "The detector system of the KATRIN experiment - implementation and first measurements with the spectrometer," Ph.D. dissertation, Karlsruher Institut für Technologie (KIT), 2014. [Online]. Available: http://nbn-resolving.org/urn:nbn:de:swb:90-427724

[46] B. Leiber, "Investigations of background due to secondary electron emission in the KATRIN-experiment," Ph.D. dissertation, Karlsruher Institut für Technologie (KIT), 2014. [Online]. Available: http://nbn-resolving.org/urn:nbn:de:swb:90-424154

[47] A. Beglarian, F. Glück, A. Huber, and T. Thümmler, "Single layer air coils at 175 a," 2016, mainspectrometer, Message ID: 1753. [Online]. Available: https://neutrino.ikp.kit.edu:8080/main-spectrometer/1753

[48] F. Fränkle, "Personal communication."

[49] S. Reimer, "Ein elektrostatisches dipolsystem zur eliminierung von ionen in der dps2-f des katrin experimentes," Ph.D. dissertation, Karlsruher Institut für Technologie (KIT), 2009.

[50] F. Glück, "Electrons and ions in katrin sts," *internal KATRIN document*, 2010.

[51] ——, "Positive ions from wgts," *internal KATRIN document*, 2015.

Danksagung

Abschließend möchte ich noch die Personen danken, die mich während des Studiums unterstützt haben und immer für mich da waren. Diese Abschlussarbeit wäre nicht möglich gewesen ohne:

- Prof. Dr. G. Drexlin dafür, dass mir diese interessante Masterarbeit angeboten wurde und für die hilfreichen Tipps während den SDS Analyse-Meetings.
- Prof. Dr. W. de Boer dafür, dass er freundlicherweise das Korreferat übernommen hat.
- Dr. Fabian Harms für die sehr gute Betreuung und die vielen Hilfestellungen während der Masterarbeit. Die gemeinsamen Diskussionen waren sehr lehrreich und haben maßgeblich zum Gelingen dieser Abschlussarbeit beigetragen. Für die vielen Korrekturen der einzelnen Kapitel bedanke ich mich auch herzlich.
- Dr. Ferenc Glück für die Hilfe bei physikalischen Problemen und für die nette Zeit im gemeinsamen Büro.
- Daniel Hilk für die Einführung in das Simulationsprogramm und die Hilfe bei auftretenden Fragen bezüglich Simulationen.
- Dr. Stefan Groh für die Hilfe bezüglich C++ und bei der Erstellung von weiteren Generatoren für Kassiopeia.
- Nikolaus Trost für die Einführung in Python und dafür, dass ich immer einen Ansprechpartner hatte wenn Simulationen schief gingen oder Analysecodes nicht funktionierten.
- Agnes Seher, Axel Müller, Dr. Florian Fränkle, Dr. Moritz Ehrhard und allen anderen Mitarbeitern der KATRIN-Gruppe für die schöne gemeinsame Zeit.
- Meiner Physik-Gruppe dafür, dass ich von Anfang an Anschluss gefunden hab und ihr mich ertragen habt. Die tolle gemeinsame Zeit während dem Studium hat mich sehr geprägt und mich menschlich weiterentwickelt. Ich hoffe ihr fühlt euch hiermit angesprochen, auch wenn ich nicht explizit Namen nennen kann, da die Liste sonst ausartet.
- Alle oben genannten und die, die ich vergessen habe (tut mir sehr leid), erhalten an dieser Stelle nochmal an herzliches Dankeschön.

Ein besonderer Dank gilt auch meinen Eltern Sarwat Mumtaz und Nasir Ahmad und meiner Familie, ohne deren Hilfe mein Studium gar nicht erst möglich gewesen wäre. An dieser Stelle danke ich auch meinen Schwiegereltern, die gerade während stressigen Zeiten für Entspannung gesorgt haben.

Meiner liebevollen Ehefrau Naima Bhatti danke ich für ihre unermüdliche Hilfe und ihren Beistand. Durch sie konnte ich meine Motivation bis zum Schluss behalten.

Finally i would like to thank Hazrat Mirza Masroor Ahmad Khalifat-ul-Masih the fifth for his guiding and endless prayers.